Available online at www.keaipublishing.com/en/journals/journal-of-magnesium-and-alloys/

ScienceDirect

Journal of Magnesium and Alloys 13 (2025) 3798–3818

www.elsevier.com/locate/jma

Full Length Article

Microstructure evolution and corrosion behavior of TIG welded joint of a new Mg–Gd–Nd–Zn–Zr alloy during post-weld heat treatment ☆

Xin Tong, Qiman Wang, Guohua Wu*, Fangzhou Qi, Junmin Zhan, Liang Zhang

National Engineering Research Center of Light Alloy Net Forming and State Key Laboratory of Metal Matrix Composites, School of Materials Science and Engineering, Shanghai Jiao Tong University, Shanghai 200240, China

Received 2 December 2023; received in revised form 6 April 2024; accepted 15 April 2024
Available online 3 May 2024

Abstract

The corrosion behavior of the tungsten inert gas (TIG) welded Mg–3Nd–3Gd–0.2Zn–0.5Zr alloy with different post-weld heat treatments was systematically investigated. The results show that the corrosion resistance of the sand-cast base material (BM) was inferior to that of the fusion zone (FZ), which was attributed to the larger grain size and exacerbated galvanic corrosion caused by coarser Mg_3(Nd, Gd) eutectic phases and numerous β precipitates. It is found that post-weld solid-solution (T4) treatment could significantly enhance the corrosion resistance of the joint due to the dissolution of the cathodic second phases and the denser protective film abundant in RE oxides generated in corrosive solution. The precipitation of nanosized phases and Zn–Zr clusters would slightly increase the susceptibility to localized corrosion of the peak-aged (T6) joint. As the main corrosion products, MgO and $Mg(OH)_2$ are distributed throughout the whole corrosion film, while RE oxides and RE hydroxides are mainly distributed in the inner layer, which can be explained by inward oxidation and replacement reactions between RE elements and MgO/$Mg(OH)_2$. Based on the composition and structure of the corrosion product film, a physical model has been proposed for depicting the microstructure evolution associated with the corresponding corrosion behavior of the joints. This work could promote the applications of welded Mg–RE alloy joint in some corrosion environments.

Keywords: TIG welding; Mg–Gd–Nd alloy; Heat treatment; Microstructure evolution; Corrosion behavior.

1. Introduction

Mg rare-earth (Mg–RE) alloys present many advantages including low density, high specific strength, good creep resistance and desirable corrosion resistance, which make the alloys attractive for some engineering applications in aerospace and aviation industries [1–4]. Among them, WE series (Mg–Y–RE–Zr) alloys are the most commercially available and have been extensively studied over the past decade [5–7]. However, Y_2O_3 inclusions are inevitable during the casting process due to the extremely high oxygen affinity of Y, which is unfavorable to the castability of the alloy [8–10]. Therefore, extensive researches have focused on the development of high-performance Mg–RE alloys without Y addition, e.g. EV31 [11,12] and EV33 [13–15] alloys. In our previous studies, EV33 (Mg–3Nd–3Gd–0.2Zn–0.5Zr) alloy exhibits comparable mechanical properties with WE43 alloy. The tensile strength and elongation of peak-aged EV33 alloy can reach up to 322 MPa and 6.5%, respectively [16,17]. Moreover, EV33 alloy also shows promising corrosion resistance and fatigue performance [13,18]. It is worth mentioning that all the latest reports on EV33 alloy are related to the research on casting method. However, with the increasing demands of complex structures and large scale of the spacecraft components, it is difficult to meet the requirements through conventional casting process.

Welding is believed to be one of the essential forming methods for EV33 alloy to manufacture large-scaled aerospace components with complex structures, such as the cabin and fuel tank of some spacecraft. Tungsten inert gas

☆ Peer review under the responsibility of Chongqing University.

* Corresponding author.
E-mail address: ghwu@sjtu.edu.cn (G. Wu).

https://doi.org/10.1016/j.jma.2024.04.019

(TIG) welding is the most widely utilized due to its high flexibility and economic efficiency [19–21]. Therefore, the study of TIG welding on EV33 alloy is in critical need for broadening its applications in related key areas. In our previous studies, TIG-welded EV33 alloy fabricated using pulse current exhibits superior comprehensive tensile properties with a joint efficiency of ~88% [14]. The tensile strength of the joint without heat treatment reaches 220 MPa and the elongation exceeds 11%, which shows a great prospect in industrial applications.

In order to further promote the application of welded EV33 alloy in some possible corrosive environments in aerospace (etc. storage tanks), it is necessary to investigate the corrosion resistance of TIG-welded EV33 alloy joints. However, the existing investigations only focused on the corrosion properties of as-cast Mg–RE alloys [18], whereas no relevant works regarding the welded joints have been reported. It is worth mentioning that the microstructure of welded joint is quite different from that of as-cast alloy [22–25], which may result in a completely different corrosion behavior. For example, as compared to the base material (BM) of cast Mg–10Gd alloy, the grain size of the fusion zone (FZ) of the electron beam welded joint significantly decreased from 75 μm to ~3 μm, accompanied by the precipitated Mg_5Gd phases within the grain interior [22]. Zhang et al. [12] fabricated EV31 alloy joint by laser welding, and found that the FZ exhibits a fine and uniformly distributed cell structure containing Mg_3Nd metastable phase at grain boundaries. In the TIG welding of EV33 alloy [14], the grains in the FZ were remarkably refined attributed to the growth restriction effect, and the Mg_3(Nd, Gd) eutectics in FZ exhibit a fine and uniform distribution. The microstructure of the welded joint could greatly affect the corrosion susceptibility by changing the galvanic corrosion and the structure of corrosion product film [18]. In this regard, the influence of microstructure evolution on the corrosion performance of the joint deserves considerable attention.

In addition, as a typical age-hardening RE-containing magnesium alloy, post-weld heat treatment is required to regulate the type and distribution of RE-containing phases to improve the mechanical properties of EV33 alloy joints [13,16,17]. During heat treatment, the dissolution of eutectics and the precipitation of nano-scale RE-containing phases may exert a great influence on micro-galvanic corrosion, thus affecting the corrosion performance of the EV33 alloy joints. Moreover, it has also been reported that the corrosion film with different compositions and morphology could be generated during the immersion test after different heat treatment, which also plays an important role in the corrosion performance [26–31]. For instance, Liang et al. [28] found that a compact yellowish corrosion layer was formed on the T4-treated GW73K alloy after the immersion test in NaCl solution, which effectively inhibited the local corrosion. Based on the above studies, it can be speculated that post-weld heat treatment may also be of great significance in optimizing the corrosion performance of EV33 alloy joints. Currently, much attention has been paid to the mechanical properties of Mg–RE alloy joints, while the effect of the post-weld heat treatments on the corrosion behavior has never been reported before.

This work aims to investigate the effect of microstructure evolution on the corrosion behavior of EV33 alloy joints with different heat-treated (solid-solution and peak-aged) states, and reveal the corrosion behavior of different regions (including FZ and BM) of the joint. Detailed analyses of the composition and structure of corrosion product film were performed, and the possible reactions during the immersion test have been discussed for a better understanding of the formation mechanisms of the protective layer. It is believed that this work could promote the applications of welded Mg-RE alloys in some corrosion environments.

2. Experimental procedure

2.1. Material preparation

The as-received EV33 plates with the dimension of $80 \times 32 \times 3$ mm^3 were prepared by low-pressure sand casting. Under the protection of mixed gas (99 vol% CO_2 + 1 vol% SF_6), commercial pure Mg, pure Zn, Mg–90Gd, Mg–90Nd, and Mg–30Zr (wt%) master alloys were melted in resistance furnace, and the detailed melting process has been provided in our previous work [14]. The actual composition of the base material (BM) and the filler rod was determined by Inductively Coupled Plasma-Atomic Emission Spectroscopy (ICP-AES), as listed in Table 1. Two EV33 plates were joined by the TIG welding using the AC-TIG welding machine (Rehm INVERTIG.PRO digital 450 AC/DC). The schematic of the welding process is shown in Fig. 1a, and the welding parameters are presented in Table 2. The post-weld solution treatment (T4 treatment) process is 480 °C × 6 h + 520 °C × 2 h + 540 °C × 1 h, followed by water quenching. Note that the multistage solution treatment is always used to realize a better dissolution of the eutectics and inhibit the abnormal grain coarsening in FZ, as reported in the previous research on Mg–RE alloy TIG-welded joint [23]. Finally, the obtained T4-treated joint was isothermally aging (T6 treatment) at 200 °C for 14 h, which was selected based on the age-hardening curve. The immersion test and electrochemical test were conducted to evaluate the corrosion properties of the welded samples, and the sampling positions and dimensions are illustrated in Fig. 1b. The samples used for immersion experiments included the area from FZ to BM to study the corrosion performance of the whole joint.

2.2. Microstructure characterization

The specimens were mechanically ground, polished, and finally etched in an etching reagent consisting of 10 mL acetic acid, 4 g picric acid, 75 mL ethanol, and 10 mL water. The microstructure and corrosion morphologies of the specimens were characterized by optical microscopy (OM, Carl Zeiss Axivoert 40), scanning electron microscopy (SEM, NOVA NanoSEM 230) equipped with energy dispersive X-ray spectroscopy (EDS), and laser scanning confocal microscopy

Table 1
Chemical composition (in wt%) of the base material and the filler rod.

Materials	Nd	Gd	Zn	Zr	Mg
Base material	3.05	2.98	0.24	0.49	Bal.
Filler rod	3.01	2.97	0.25	0.49	

Table 2
The welding parameters of TIG welding of EV33 alloy.

Welding method	Current (A)		Frequency (Hz)	Welding speed (mm/min)	Wire feeding speed (mm/min)	Welding voltage (V)
	I_B	I_P				
TIG	140	180	10	180	300	12

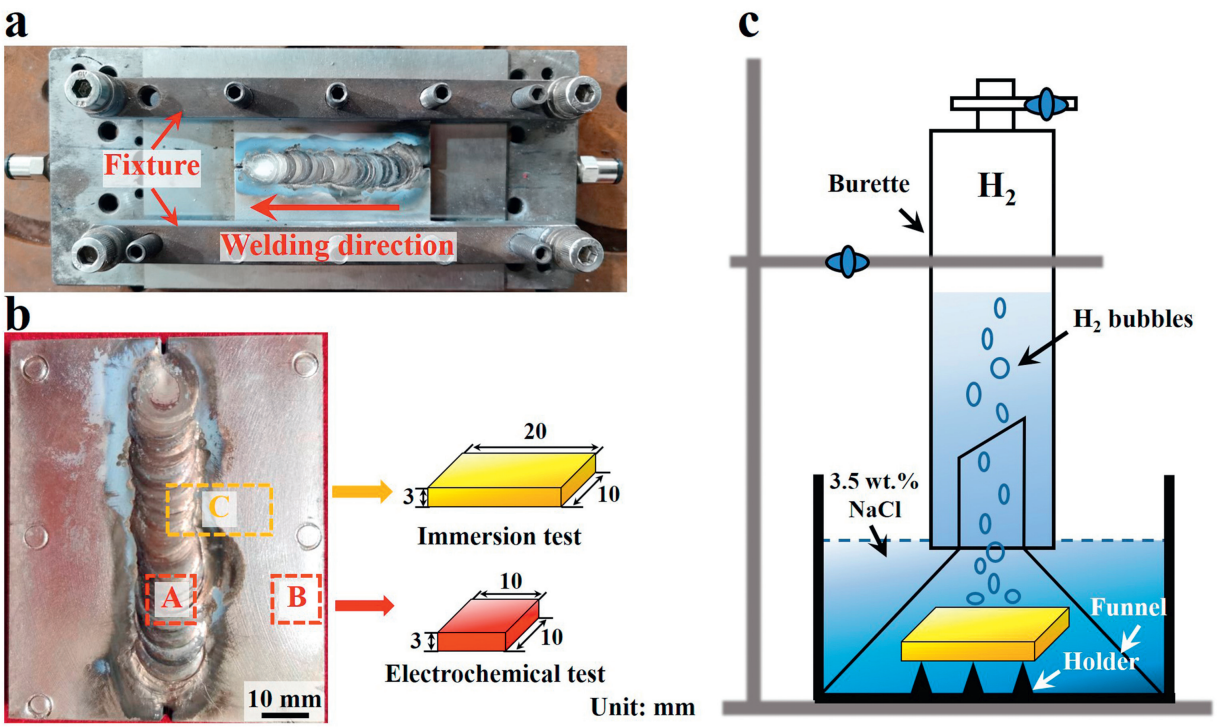

Fig. 1. Schematic of the (a) welding fixture, (b) the sampling positions and dimensions of the samples used for immersion and electrochemical tests, and (c) the set-up used for the hydrogen evolution test.

(LSCM, KC-H020). The precipitates in the center of FZ in the T6 state were revealed by the transmission electron microscope apparatus (TEM, FEI Talos F200X G2) to analyze the microstructure evolution during the aging process. The X-ray diffraction (XRD, Rigaku Ultima IV) and X-ray photoelectron spectroscope (XPS, Thermo Scientific K-Alpha) were used to characterize the corrosion products composition. The relative Volta potential difference (VPD) between the α-Mg matrix and second phases was measured by scanning Kelvin probe force microscopy (SKPFM, BRUKER Dimension FastScan) under the tapping mode. The corrosion products film was analyzed using time of flight secondary ion mass spectroscopy (ToF-SIMS, IONTOF ToF-SIMS 5–100) at a pressure of 1×10^{-9} mbar. In addition, the Gibbs free energy changes (ΔG_T) of the involved reactions between RE elements and MgO/$Mg(OH)_2$ were calculated using the thermochemical software FactSage 6.2.

2.3. Immersion tests

The samples with the dimension of 20 × 10 × 3 mm^3 (Fig. 1b) were used in the weight loss and hydrogen evolution tests. The polished specimens were weighted and then all the surfaces of the specimen were fully exposed in 3.5 wt% NaCl solution for 24 h at 25 ± 1 °C for immersion test. During immersion, the evolved H_2 was collected in the burette through a funnel above the specimens, as illustrated in Fig. 1c. The hydrogen evolution volume V_H (mL/cm^2) and the hydrogen evolution rate P_H (mm/y) were calculated as follows [18,32]:

$$V_H = \frac{\Delta V}{A} \quad (1)$$

$$P_H = \frac{2.088\ V_H}{t} \quad (2)$$

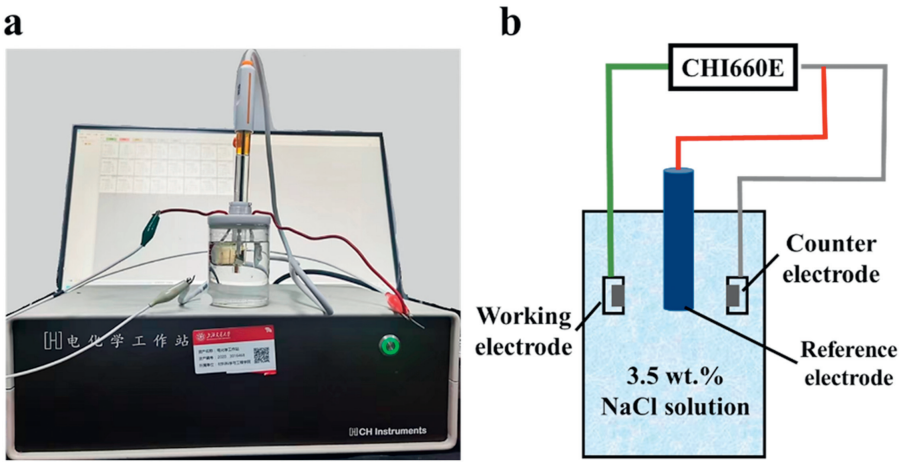

Fig. 2. The set-up for electrochemical measurement: (a) electrochemical station used in this study, (b) schematic of the three-electrode system.

Table 3
The parameters of electrochemical measurements.

Item	Initial E (V)	Final E (V)	Frequency range (Hz)	Amplitude (V)	Scan rate (mV/s)	Quiet time (s)	Sensitivity (A/V)
EIS	−1.6	—	1×10^{-2}–1×10^{5}	0.01	—	2	1×10^{-6}
Tafel	−1.9	−1.4	—	—	0.5	2	1×10^{-6}

where ΔV (mL) is the amount of evolved H_2, A (cm^2) represents the surface area of the specimen, and t (day) is the total immersion time.

After immersion for 24 h, the samples were ultrasonically cleaned in chromate acid (50 g CrO_3, 5 g $AgNO_3$, and 250 mL deionized water) for 10 min (~25 °C), dried and weighted to calculate the weight loss ΔW (mg). The weight loss rate P_W (mm/y) is calculated as follows [33]:

$$P_W = \frac{2.10\ \Delta W}{At} \tag{3}$$

2.4. Electrochemical measurements

The electrochemical behavior of the specimens was investigated using a CHI660E electrochemical workstation in 3.5 wt% NaCl solution at 25 ± 1 °C, as shown in Fig. 2. A three-electrode system was used, with a platinum plate as the counter electrode, a saturated calomel electrode (SCE) as the reference electrode, and the tested sample (exposure area of 1 cm^2) as the working electrode. The electrochemical impedance spectrum (EIS) measurement was performed after immersion in the solution for 3600 s to reach a relatively stable open circuit potential (OCP). The detailed parameters of EIS and Potentiodynamic polarization (Tafel) measurement are illustrated in Table 3. The EIS data were fitted by software Zsimpwin. The corrosion current density (i_{corr}) was obtained by Tafel extrapolation of the cathodic branch of the polarization curve. All experiments were repeated for three times to ensure the accuracy of the results.

3. Results

3.1. Microstructure evolution

Fig. 3 displays the optical microstructures of the as-welded joint. It can be seen from the low-magnification image in Fig. 3a that there exist no obvious welding defects such as voids and cracking in the joint. In addition, remarkable differences in the microstructure can be found in the joint, and a fusion line can also be observed between FZ and BM. Enlarged images of each region in Fig. 3a are shown in Fig. 3b–d. The FZ is characterized by equiaxed grains (average grain size is ~8.2 μm,) and uniformly distributed eutectics in small sizes. In addition, it can be seen that the heat affected zone (HAZ) exhibits an approximate grain size (47.6 μm) with the BM (45.2 μm). This is because a grain boundary pinning effect is achieved by the thermostable RE-containing eutectics, and thus the grain coarsening of HAZ is inhibited under the welding heat. As a result, HAZ is hard to be clearly distinguished in the cross-section of the joint in Fig. 3a. It can be found that the effect of HAZ on the corrosion behavior of the joints is negligible, and the current study mainly focused on the microstructural evolution and corrosion behavior of FZ and BM.

Fig. 4 presents the SEM micrographs of FZ and BM in the EV33 alloy joints with different heat-treated states. As shown in Fig. 4a and b, numerous eutectics, which have been identified as Mg_3(Nd, Gd) phases in previous studies [14,17,18], are distributed along the grain boundaries in the as-welded joint. Moreover, in the grain interior of BM, a large quantity of plate-shaped β precipitates can be found (Fig. 4b). After

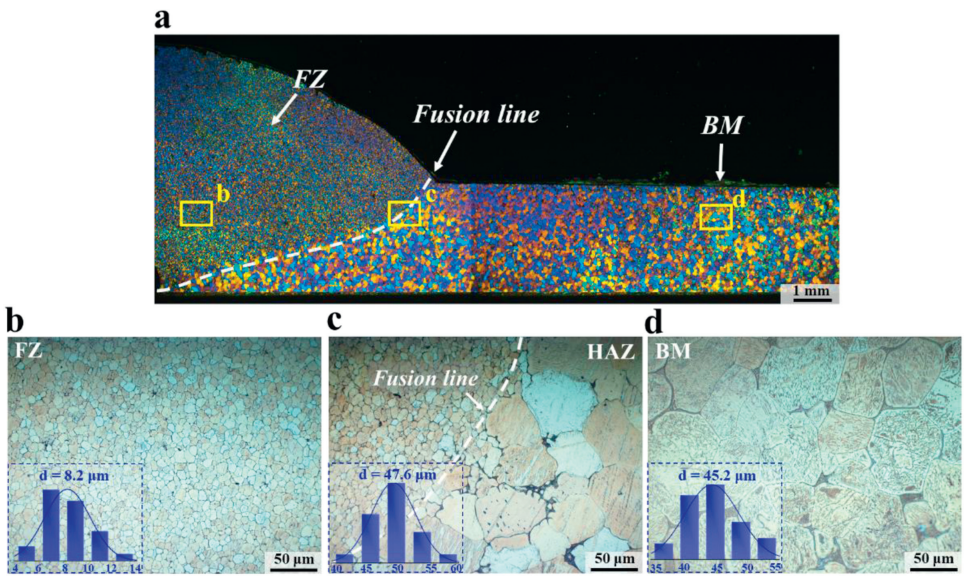

Fig. 3. Optical micrographs of the TIG joint of sand-cast EV33 alloy: (a) the whole welded joint, and (b)–(d) the magnified views of the boxed regions marked in (a).

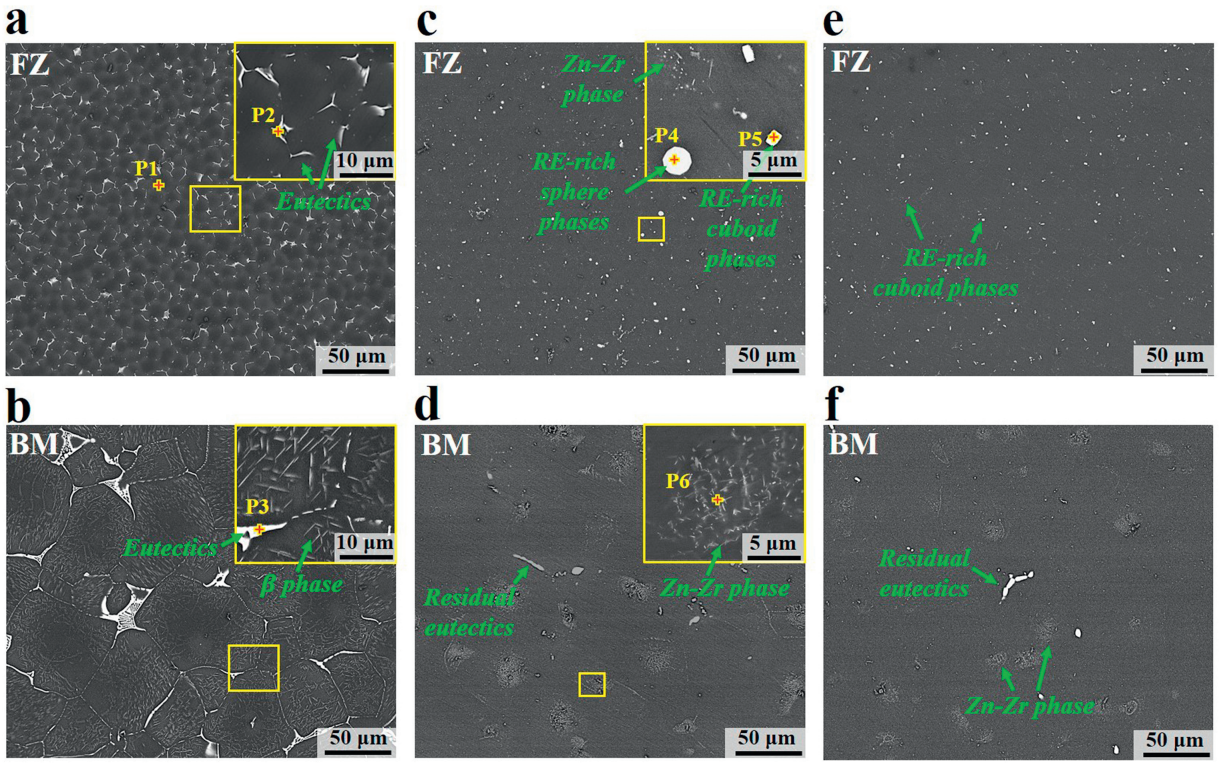

Fig. 4. SEM micrographs of the FZ and BM in EV33 alloy joints with different heat-treated states: (a and b) as-welded, (c and d) T4, (e and f) T6.

T4 treatment, most of the eutectics are dissolved and numerous rod-shaped dispersoids are formed. The EDS analyses in Table 4 indicate that the rod-shaped particles are the clusters of the Zn–Zr phase, which is also accordant with the published literatures [17,34]. It is worth mentioning that the Zn–Zr cluster shows a much smaller size in FZ. In addition, fine particles with sizes of 1∼3 μm are visible in FZ with T4 and T6 treatments. As shown in Fig. 4c and e, the cuboid phase is mainly rich in Gd element while the sphere phase is mainly rich in Nd element. As compared to FZ, there are a few eutectics remaining in BM, as shown in Fig. 4d and f.

To further clarify the precipitation behavior during the ageing process, TEM observation was carried out with the incident beam parallel to $[0001]_\alpha$ direction, as shown in Fig. 5. The lenticular $\{11\bar{2}0\}_\alpha$ platelets with a dense distribution are observed in Fig. 5a. Extra diffraction spots can be found at

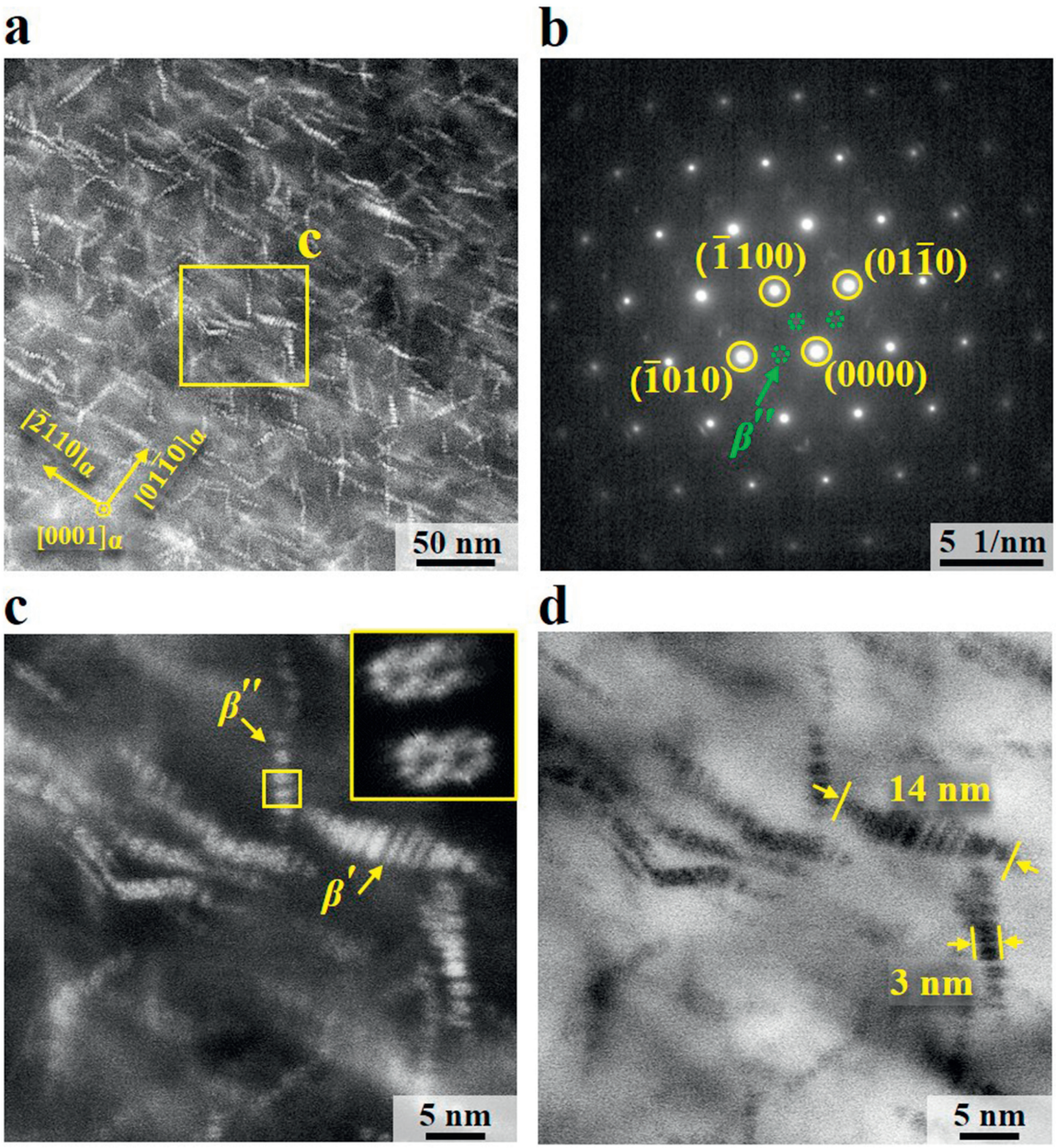

Fig. 5. TEM micrographs of FZ in T6-treated joint: (a) HAADF- STEM image, (b) the selected area electron diffraction (SAED) pattern, (c) the enlarged image of the rectangular region in (a), (d) bright field (BF) image corresponding to (c). (The incident beam is along $[0001]_\alpha$ zone axis).

Table 4
EDS point analyses (in at.%) in Figs. 4 and 11.

Point	Mg	Nd	Gd	Zn	Zr	O
1	99.25	0.31	0.27	0.05	0.12	–
2	77.26	14.62	5.11	3.01	–	–
3	86.94	8.12	2.71	2.23	–	–
4	54.90	37.63	3.56	3.91	–	–
5	43.57	19.09	35.36	1.98	–	–
6	92.12	0.29	0.21	2.56	4.82	–
7	39.98	0.32	0.21	0.88	0.12	58.49
8	27.04	2.14	2.32	0.75	0.18	67.57

1/2 $(10\bar{1}0)_{\alpha\text{-Mg}}$ positions in selected area electron diffraction (SAED) pattern in Fig. 5b. Based on this orientation relationship, these fine lenticular precipitates can be identified as β'' phases (Mg_3RE, $D0_{19}$, $a = 0.64$ nm and $c = 0.52$ nm) [35]. From the enlarged image (Fig. 5c), the β'' phases are characterized with hexagonal arrays consisting of six columns of RE atoms. The bright field (BF) image in Fig. 5d further displays that these precipitates exhibit a thickness of ~3 nm and a diameter of ~14 nm. Additionally, there are also some lenticular prismatic β' phases in the sample, which has been reported in the previous studies on Mg–Gd–Nd alloys [17,36,37]. Therefore, β'' and β' are the main strengthening phases in the aged EV33 alloy.

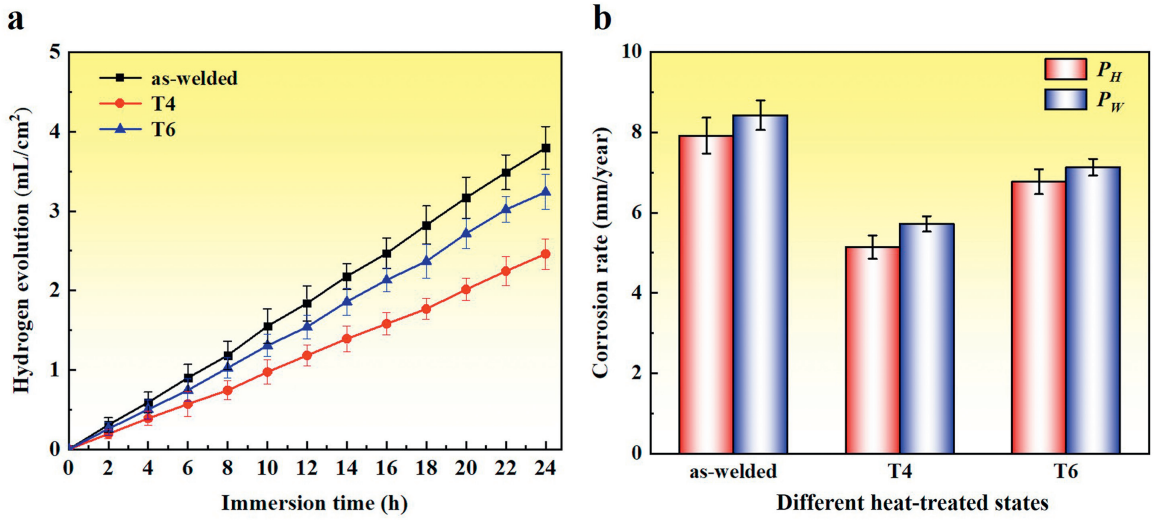

Fig. 6. Hydrogen evolution test (a) and corrosion rates derived from weight loss and hydrogen evolution (b) of EV33 alloy joints with different heat-treated states in immersion experiment.

3.2. Corrosion properties

Fig. 5 shows the hydrogen evolution (Fig. 6a) and average corrosion rate (Fig. 6b) calculated by P_W and P_H of EV33 alloy joints with different heat-treated states after immersion for 24 h. It can be found that the hydrogen evolution increases linearly with the increasing immersion time, and the as-welded joint exhibits the highest amount of hydrogen evolution. As shown in Fig. 6b, the P_W of the as-welded sample decreases from 8.43 to 5.72 mm/y after T4 treatment, and then increases to 7.13 mm/y after T6 treatment, indicating that the T4-treated sample has the highest corrosion resistance. In addition, the P_H of as-welded, T4- and T6-treated joints are 7.92, 5.14, and 6.77 mm/y, respectively, which is in accordance with the change tendency of P_W. It is worth noting that the P_H of all the joints is slightly lower than P_W, maybe due to the dissolution of H_2 in solution or the shedding of non-corrosive areas during the cleaning process. Comprehensively considering the P_W and P_H, the corrosion resistance increases in the order of T4 > T6 > as-welded.

Fig. 7 presents the potentiodynamic polarization curves and the corresponding fitted parameters. In general, the cathodic branch is related to the hydrogen evolution in an aqueous solution, and the anodic branch refers to the dissolution of the α-Mg matrix [38]. The cathodic branch exhibits the extensive liner Tafel region, which demonstrates the relatively steady hydrogen evolution and corrosion rate. For the anodic parts of the curve, no significant passivation stage could be observed, indicating it is difficult to form a passivating film on the joint surface [39]. Among the tested samples with different heat treatments, the T4-treated specimens always present more positive corrosion potential (E_{corr}) and lower corrosion rate (i_{corr}), suggesting their better corrosion resistances. It can be speculated that the T4 treatment is conductive to promoting the protective effect of the oxide film according to the higher E_{corr} value [40]. In addition, different regions (FZ and BM) of a welded joint usually exhibits different E_{corr} and i_{corr}, and FZ always shows a better corrosion resistance. In general, among the samples, the corrosion resistance of T4-treated FZ is the highest, while that of BM of the as-welded joint is the lowest.

Fig. 8 depicts the EIS plots of the specimens and the electrochemical equivalent circuit. From Nyquist plots of Fig. 8a, all samples consist of three well-defined loops: a high-frequency capacitive loop, a medium-frequency capacitive loop, and a low-frequency inductive loop. According to the previous studies [41–43], they represent the charge transfer reaction of surface oxide/hydroxide film at high frequency, the charge transfer reaction of the electric double layer at middle frequency, and the mass diffusion of ions through the corrosion product film at low frequency, respectively. Herein, the capacitive loop radiuses of T4-treated samples are larger than those of the as-welded and T6-treated samples, indicating that the T4 treatment could greatly improve the charge transfer resistance of the EV33 alloy joint, which is beneficial to the reduction of corrosion rate. Additionally, the FZ with a larger loop radius usually shows preferable corrosion resistance as compared to the BM within a welded joint. For the Bode plots of impedance-frequency in Fig. 8b, it can be observed that the FZ of the T4-treated joint always maintains the highest impedance modulus. In terms of Bode plots of phase angle-frequency in Fig. 8c, two wave crests and one wave trough are visible, demonstrating the presence of two capacitance loops and one inductive loop. In addition, the largest peak value and peak width of T4-treated FZ also suggest its best corrosion resistance among all the specimens [42,44].

In order to clarify the corrosion mechanism of these specimens, the equivalent circuit diagram is provided in Fig. 8d, and the fitting data are displayed in Table 5. Herein, the resistor elements of R_s, R_{ct}, and R_f correspond to the solution resistance, the charge transfer resistance, and the corrosion

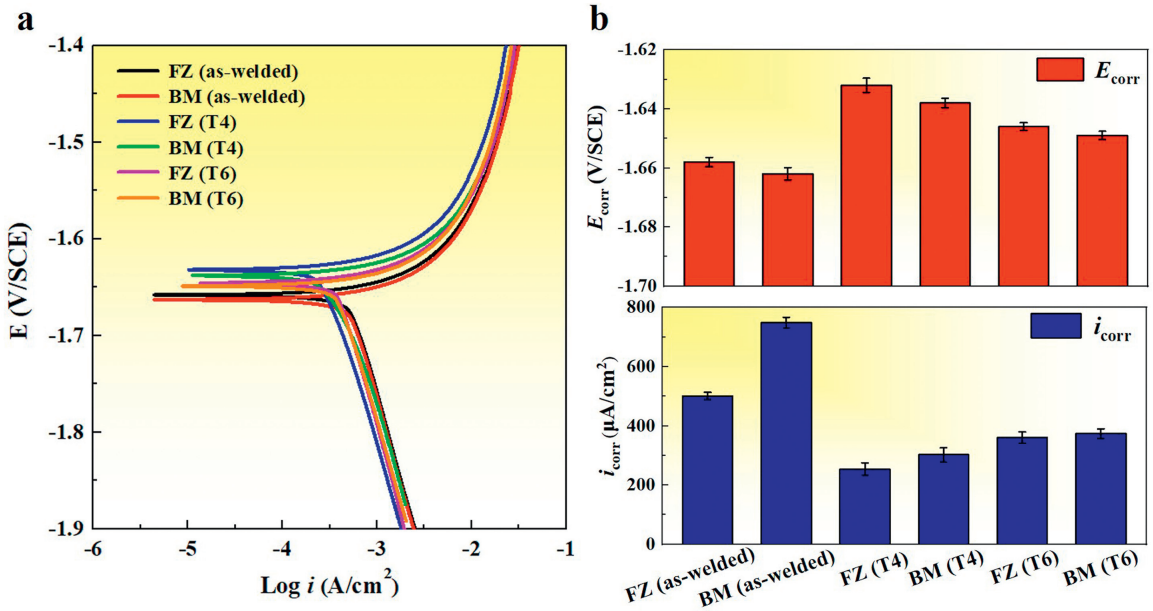

Fig. 7. Polarization teats of the FZ and BM in EV33 alloy joints with different heat-treated states: (a) potentiodynamic polarization curves, (b) E_{corr} and i_{corr} extracted from polarization curves.

Table 5
The fitting parameters related to the EIS diagram in Fig. 8.

Samples	R_s ($\Omega\cdot cm^2$)	CPE_f		R_f ($\Omega\cdot cm^2$)	CPE_{dl}		R_{ct} ($\Omega\cdot cm^2$)	R_L ($\Omega\cdot cm^2$)	L ($H\cdot cm^2$)	R_P ($\Omega\cdot cm^2$)
		$Y_{0,dl}$ ($\mu F\cdot cm^{-2}\cdot s^{n-1}$)	n		$Y_{0,f}$ ($\mu F\cdot cm^{-2}\cdot s^{n-1}$)	n				
FZ (as-welded)	8.936	6.621	0.88	220.5	7.14	0.93	37.7	87.3	1658	65.2
BM (as-welded)	7.877	6.534	0.92	188.4	7.833	0.96	38.5	84.7	1895	61.7
FZ (T4)	8.161	3.234	0.91	317.9	6.191	0.99	47.3	126.3	4790	93.8
BM (T4)	8.478	3.131	0.87	281.6	6.118	0.97	49.9	97.9	1552	75.6
FZ (T6)	8.723	4.304	0.94	242.5	6.843	0.92	41.4	95.7	1672	71.6
BM (T6)	8.561	4.814	0.91	248.9	6.259	0.94	40.4	85.6	1196	66.1

film resistance, respectively. Additionally, the constant phase elements (CPE) of CPE_f and CPE_{dl} refer to the capacitors of corrosion product film and electric double layer at the substrate/solution interface, respectively [38]. The CPE component is defined by two parameters with Y_0 and n, which represent the non-ideal capacitance and the dispersion index ranging from 0 to 1, respectively [45]. The inductance L in series with the resistance R_L denotes the rupture of the oxide film induced by the Mg^+ reaction [45,46]. The polarization resistance R_P can be used to characterize the overall corrosion resistance of the specimens, expressed as [47]:

$$\frac{1}{R_P} = \frac{1}{R_f + R_{ct}} + \frac{1}{R_L} \quad (4)$$

As shown in Table 5, there is little variation in the R_s value, since it is only dependent on the conductivity of the immersion medium. In addition, the higher R_f values of FZ (T4) and BM (T4) specimens indicate that the T4 treatment facilitates the establishment of compact corrosion film on the joint surface. On the contrary, the as-welded samples present the lowest R_f values, which may be ascribed to the lower content of RE solute participating in the formation of corrosion product film. It is worth noting that the R_{ct} of different samples varies significantly, implying that the microstructural evolution affects the charge transfer of the double layer. The larger the R_p value, the better the corrosion resistance of the joint. The R_p value of different specimens increases in the order of FZ (T4) > BM (T4) > FZ (T6) > BM (T4) > FZ (as-welded) > BM (as-welded), which further confirms the results from potentiodynamic polarization curves.

3.3. Corrosion morphology

Fig. 9 displays the macroscopic corrosion morphologies of EV33 alloy joints with different heat-treated states after immersion for 24 h. As shown in Fig. 9a, serious corrosion occurs in the as-welded joint, and the surface is almost covered by dark corrosion products. In comparison, the T4-treated joint presents superior corrosion resistance on account of its less corroded areas. In addition, the corrosion mainly occurs in the BM, and the amount of corrosion products in FZ is much lower (Fig. 9b). In terms of the T6-treated joint (Fig. 9c), the corroded area is less than that of the as-welded joint, but slightly larger than that of the T4-treated joint.

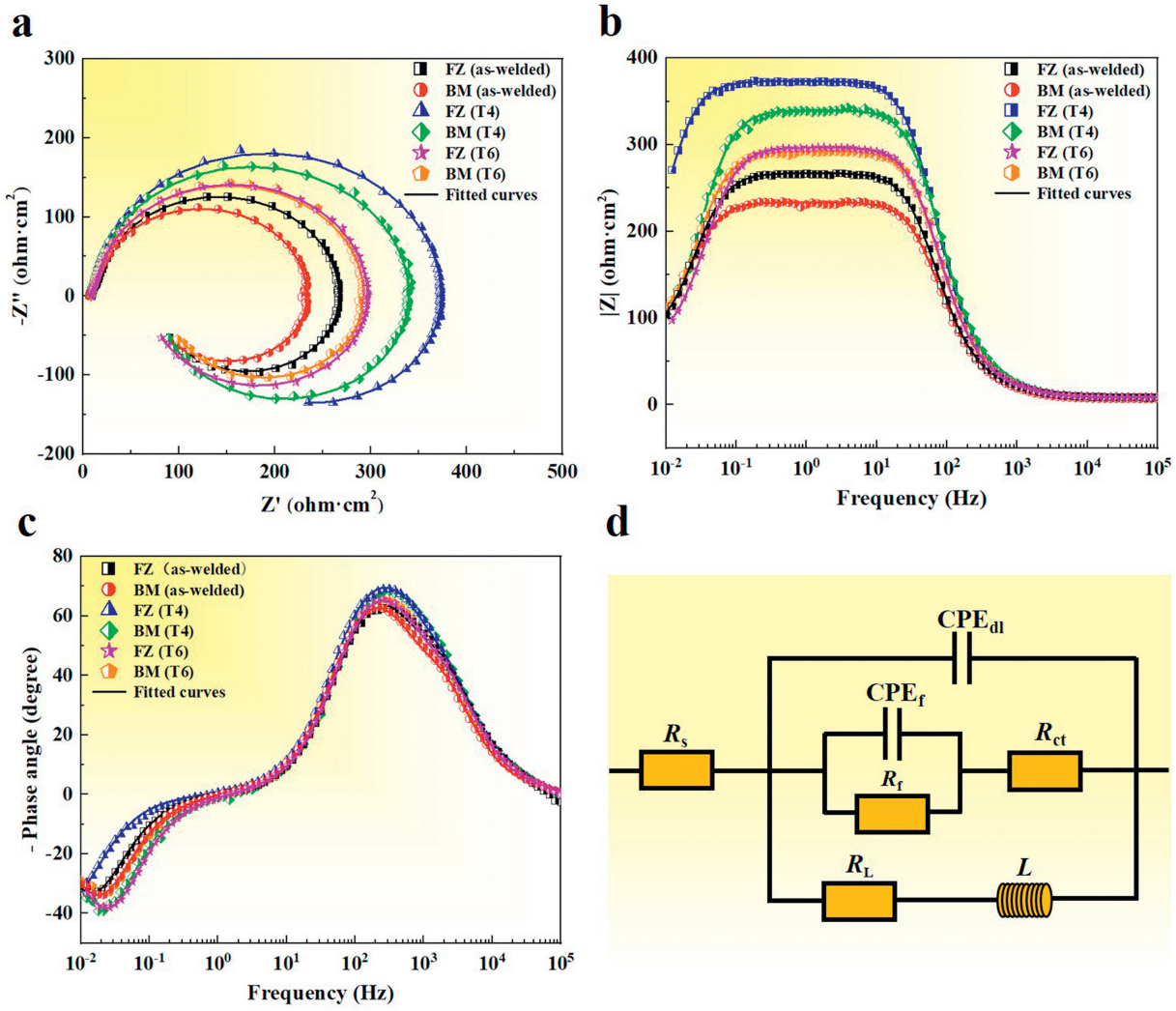

Fig. 8. EIS of the FZ and BM in EV33 alloy joints with different heat-treated states: (a) Nyquist plot, (b) |Z|-frequency plot, (c) phase angle-frequency plot, (d) electrochemical equivalent circuit.

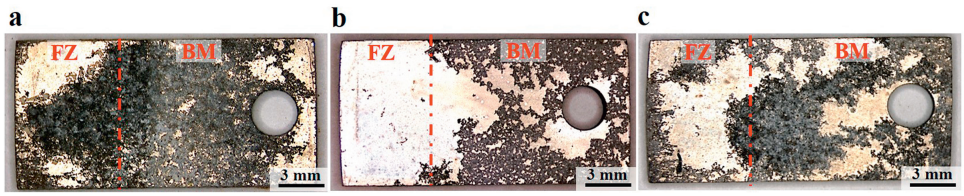

Fig. 9. Macroscopic corrosion morphologies of EV33 alloy joints with different heat-treated states: (a) as-welded, (b) T4, (c) T6.

Fig. 10 shows the 3D corrosion morphology of the EV33 alloy joints. In terms of the as-welded joint (Fig. 10a and b), some deep corrosion pits and thick oxidation film can be detected on the surface, indicating serious localized corrosion occurred in this joint. In contrast, the T4-treated joint exhibits a corrosion layer with a relatively uniform thickness, accompanied by some small local corrosion (Fig. 10c and d). As for the T6-treated joint (Fig. 10e and f), several shallow pits with a depth of around 20 μm appear on the surface, suggesting its inferior corrosion resistance to T4-treated joint. The maximum height difference (ΔH_{max}) of the joint surface is dependent on the thickness of corrosion products and the depth of corrosion pits [42]. As can be seen from Fig. 10b, d and f, the measured results of ΔH_{max} of as-welded, T4- and T6- treated samples are 93.35 μm, 60.52 μm, and 75.71 μm, respectively.

The corrosion products formed on FZ and BM after the immersion test is shown in Fig. 11. At low magnification, agglomerated particles, and micro-cracks can be observed on the surface of FZ and BM of as-welded and T6-treated joints (Fig. 11a, b, and f), while the surface of T4-treated joint is covered with dense and uniformly distributed corrosion prod-

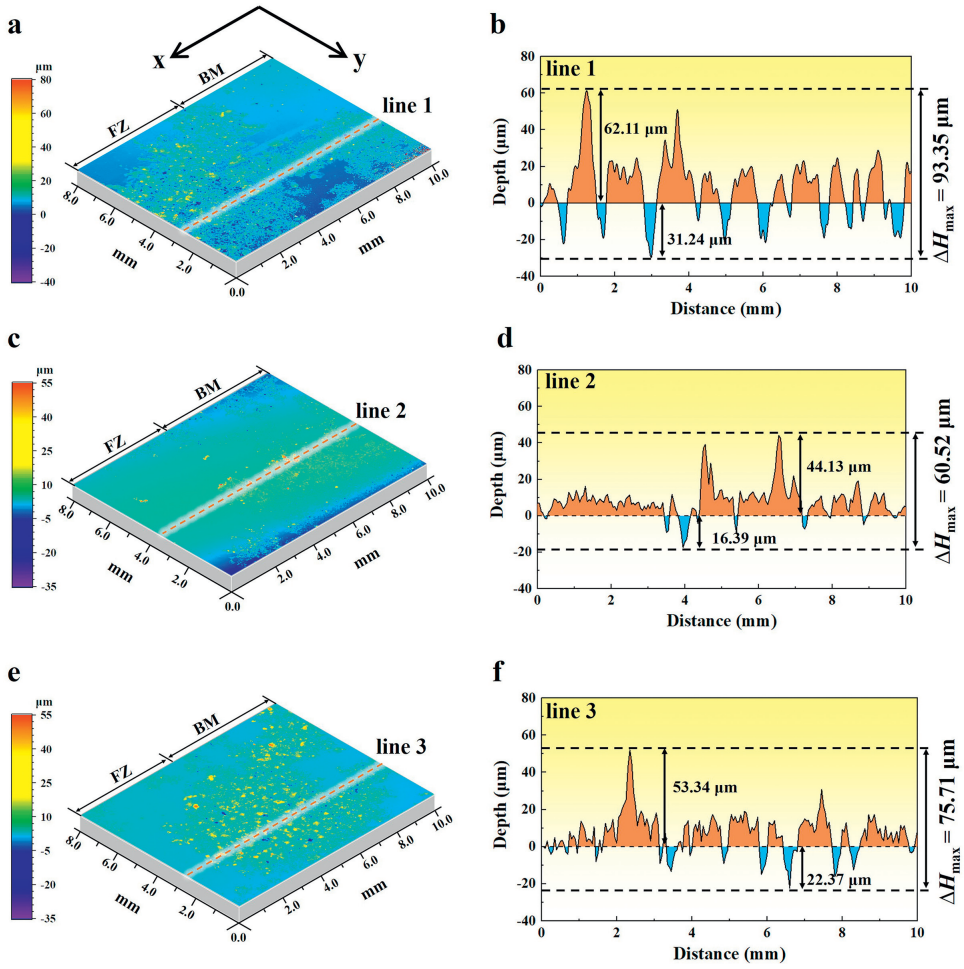

Fig. 10. 3D corrosion morphologies and corrosion depth of EV33 alloy joints with different heat-treated states: (a and b) as-welded, (c and d) T4, (e and f) T6.

ucts (Fig. 11c and d). From the magnified image at the top right corner of Fig. 11a–f, the corrosion products are usually in the morphologies of loose globular clusters (mainly in as-welded and T6 states) and dense blade-like flakes (mainly in the T4 state). In general, the compact and uniformly distributed flakes could effectively hinder Cl^- from the erosion of the inner α-Mg matrix [28,48], suggesting that the T4-treated joint may have a better corrosion resistance. The corresponding EDS mapping of as-welded BM (Fig. 11 g) indicates that the elements of O, Mg, Nd, and Gd are mainly enriched at the corrosion products (Fig. 11h). The EDS point analyses in Table 4 further confirm that the bright particle is rich in RE elements, while the dark inner layer is mainly composed of Mg-containing oxides.

Fig. 12 shows the cross-section corrosion morphologies of FZ and BM with different heat-treated states. The as-welded BM presents a non-uniform corrosion morphology, and a severe localized corrosion with a depth of ~ 89.7 μm can be observed (Fig 12b). Note that the second phases are retained in the corrosion product layer, mainly because they act as the cathode to promote the corrosion of adjacent α-Mg matrix [49]. The EDS mapping (Fig. 12c) reveals that RE elements are enriched in the second phase, and O element is penetrated deeply in the matrix. The T4-treated joint displays a relatively uniform morphology with a shallow corrosion depth (Fig. 12d and e), in which the maximum corrosion depth of FZ is only 14.5 μm. As shown in Fig. 12f and g, the corrosion depth of the T6-treated joint is greater than that of the T4-treated joint, but slightly lower than that of the as-welded joint. The corrosion pits with the depth of ~ 20.2 μm and ~22.1 μm are found in the FZ and BM, respectively.

The corrosion morphologies of the EV33 alloy joints after removal of the corrosion products are shown in Fig. 13. In terms of the as-welded joint, a great chunk of the α-Mg matrix is corroded and exfoliated, forming severe localized corrosion areas with a diameter of tens of microns (Fig. 13a and b). In comparison, the T4-treated joint shows a relatively smooth and uniform surface dominated by shallow corrosion pits (Fig. 13c and d), and the T6-treated joint exhibits a tunnel-like corrosion morphology (Fig. 13e and f). The enlarged images of the as-welded joint reveals that the α-Mg matrix near the Mg_3(Nd, Gd) eutectics is corroded preferentially, which could be ascribed to the lower Volta potential of α-Mg [18]. In addition, the β phases in the grain interior of BM may also cause the slight corrosion of the surrounding matrix, as depicted in Fig. 13b. As for T4- and T6-treated

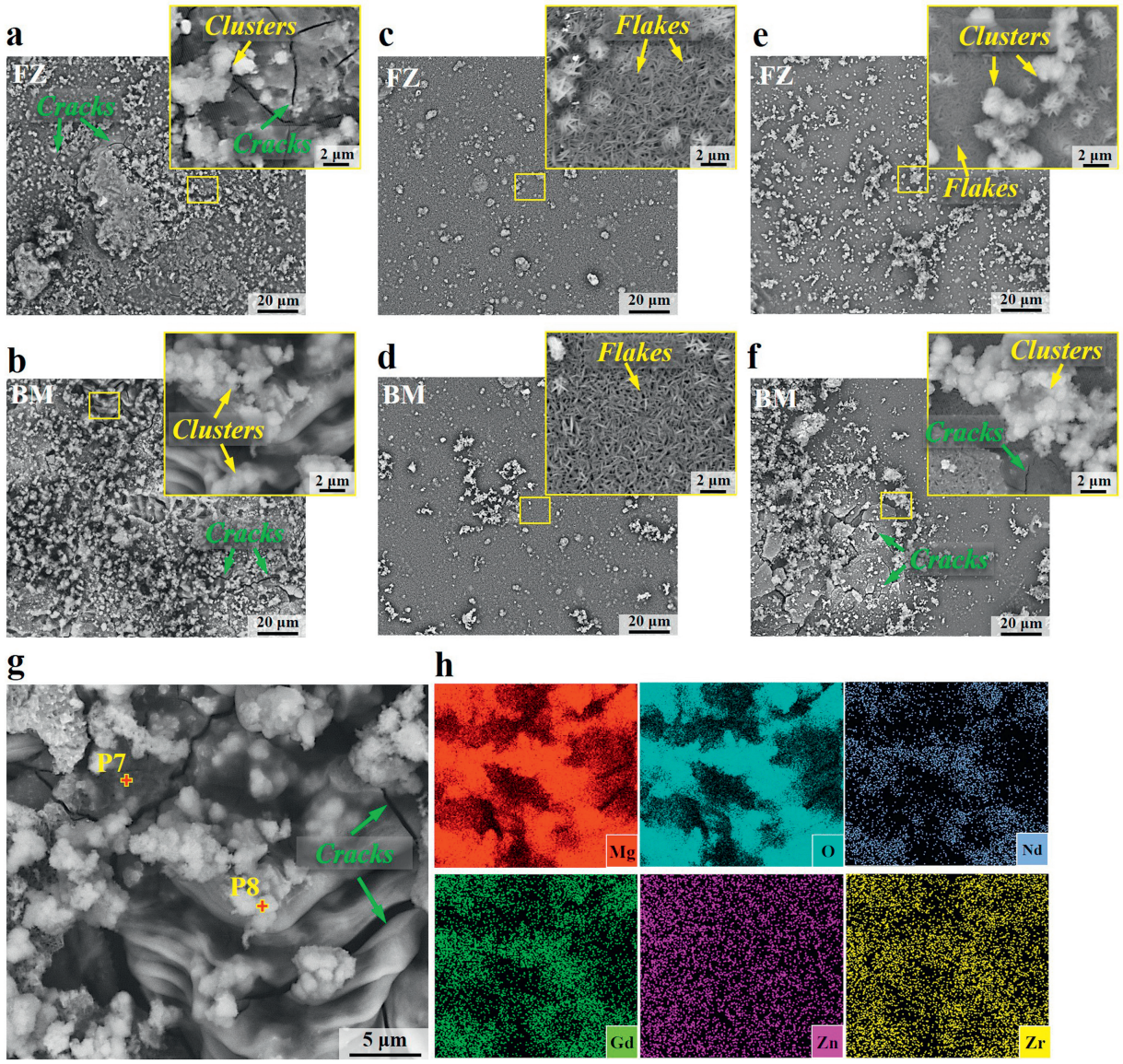

Fig. 11. Microstructure of the corrosion products of FZ and BM in EV33 alloy joints with different heat-treated states: (a and b) as-welded, (c and d) T4, (e and f) T6. (g) and (h) is the enlarged view and EDS mapping of the boxed region in (b).

joints, numerous small corrosion pits (~2 μm) can be observed in FZ, which may be resulted from the detachment of the RE-rich cuboid phases. Moreover, localized corrosion areas also exist near the Zn–Zr phase in BM (Fig. 13d and f).

3.4. Corrosion products analysis

The XRD patterns of corrosion products of FZ with different heat-treated states are shown in Fig. 14. The result reveals that $Mg(OH)_2$, Gd_2O_3 and Nd_2O_3 are the main components of corrosion products. Meanwhile, all samples exhibit the peaks of $MgCO_3{\cdot}3H_2O$, which may be generated by the reaction between $Mg(OH)_2$ and the CO_2 dissolved into the corrosive solution [47]. In addition, the small peaks corrosponding to ZnO and ZrO_2 can also be found in the spectra, as illustrated in Fig. 14b. According to the position and intensity of diffraction peaks, the content of corrosion products in the as-welded joint is significantly higher than that in the T4- and T6-treated joints, indicating poor corrosion resistance of the as-welded joint.

Table 6
The surface chemical compositions (in at.%) of FZ with different heat-treated states.

Samples	Mg 1s	Nd 3d	Gd 3d	Zn 2p	Zr 3d	C 1s	O 1s
As-welded	21.78	0.67	0.46	0.15	0.17	29.22	47.55
T4	18.27	1.73	1.18	0.11	0.22	28.18	50.31
T6	20.72	0.71	0.58	0.13	0.10	28.12	49.64

In order to further investigate the chemical compositions of the corrosion products, XPS analysis of FZ is performed, as shown in Fig. 15 and Table 6. The survey scanning spectrum of the corrosion products (Fig. 15a) reveals the exis-

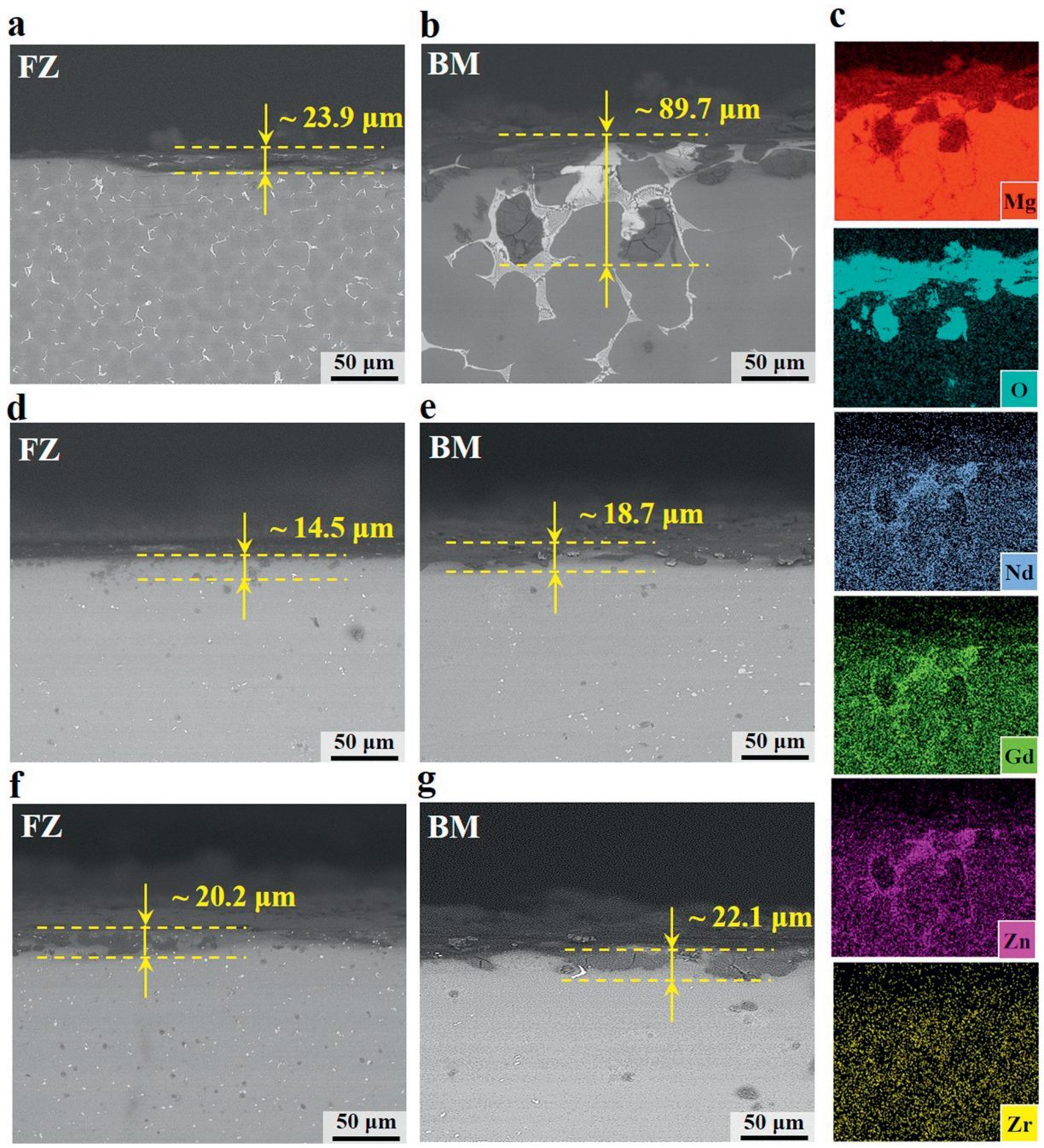

Fig. 12. Cross-section corrosion morphologies of FZ and BM in EV33 alloy joints with different heat-treated states: (a and b) as-welded, (d and e) T4, (f and g) T6. (c) is the EDS mapping of (b).

tence of Mg, Nd, Gd, Zn, Zr, O, and C elements in all samples. In Fig. 15b, the Mg 1s of all samples can be fitted into the $Mg(OH)_2$ peak at around 1303.8 eV, the MgO peak at around 1304.8 eV, and the $MgCO_3$ peak at around 1306.5 eV (Fig. 15b). In addition, three peaks with the binding energy of 978.3 eV, 981.3 eV, and 984.0 eV can be found in the high-resolution spectra for Nd 3d, indicating the existence of Nd^0, $Nd(OH)_3$, and Nd_2O_3 (Fig. 15c). Similarly, the Gd 3d spectra can be deconvoluted into three contributions centered at 1185.7 eV, 1187.9 eV, and 1190.5 eV, which correspond to the Gd^0, $Gd(OH)_3$, and Gd_2O_3, respectively (Fig. 15d).

As shown in Table 6, the RE 3d content (2.91%) of T4-treated FZ is much larger than that of as-welded and T6-treated states, maybe because more RE elements dissolved in the matrix during T4 treatment are involved in the formation of corrosion products. In addition, the contents of Zn 2p and Zr 3d in corrosion products are very low on account of the extremely low solubility of Zn and Zr in the α-Mg matrix. Table 7 presents the relative area of Nd and Gd in metallic, oxide, and hydroxide states of FZ. It can be calculated that the percentage of RE oxides (i.e. Nd_2O_3 and Gd_2O_3) in RE 3d peaks are 43.6% for the as-welded joint, 52.8% for the

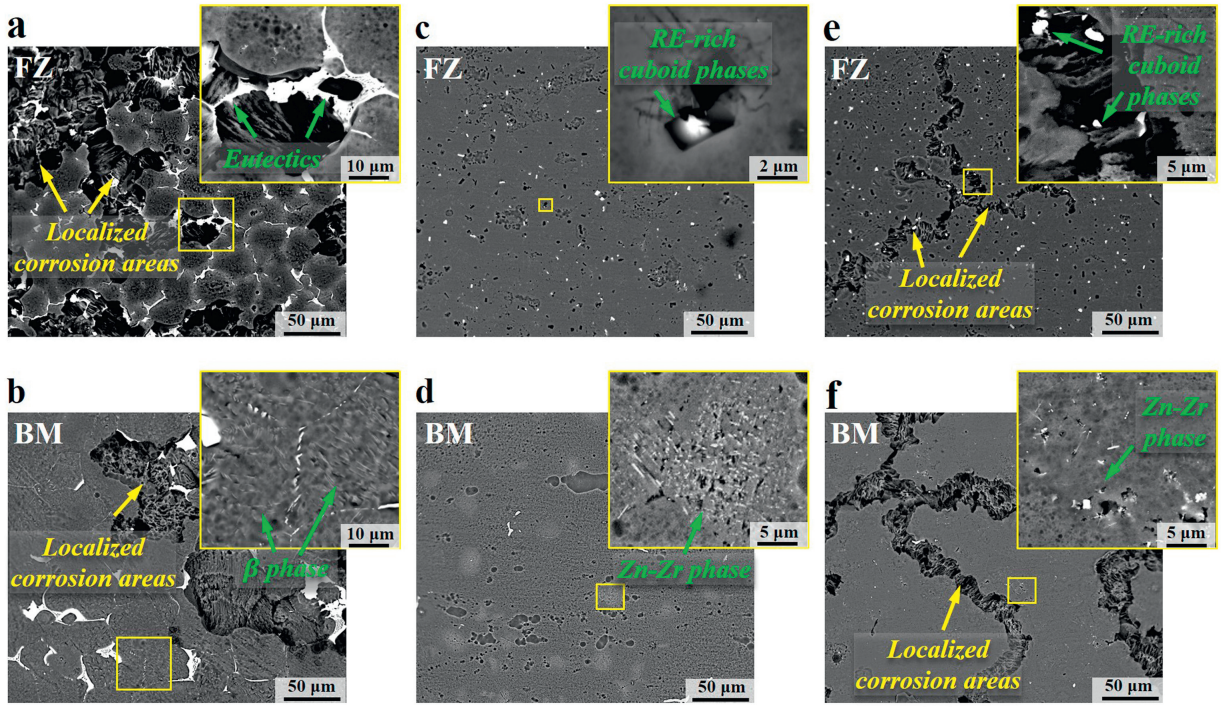

Fig. 13. Corrosion morphologies of FZ and BM in EV33 alloy joints with different heat-treated states after removal of the corrosion products: (a and b) as-welded, (c and d) T4, (e and f) T6.

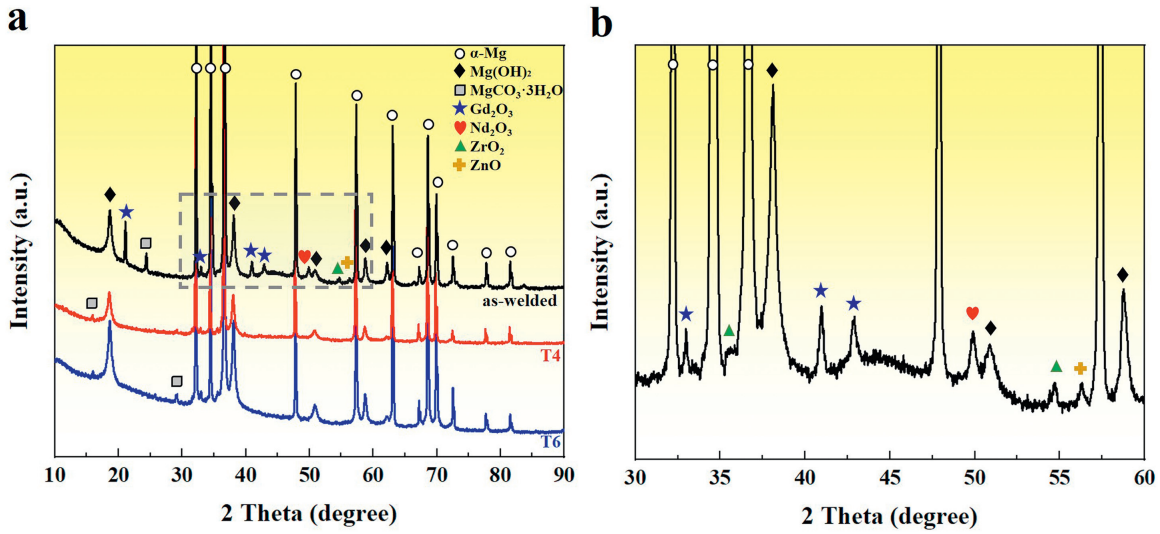

Fig. 14. XRD spectra of the FZ with different heat-treated states (a and b), and (b) is the magnified view of the square region in (a).

Table 7
The relative area of Nd and Gd in metallic, oxide and hydroxide states of FZ with different heat-treated states.

Samples	Nd 3d			Gd 3d		
	Nd^0 (978.3 eV)	Nd_2O_3 (984.0 eV)	$Nd(OH)_3$ (981.3 eV)	Gd^0 (1185.7 eV)	Gd_2O_3 (1190.5 eV)	$Gd(OH)_3$ (1187.9 eV)
As-welded	48.1	20.3	31.6	24.9	23.3	51.8
T4	45.9	23.7	30.4	21.1	29.1	48.8
T6	46.6	21.5	31.9	21.5	25.9	52.6

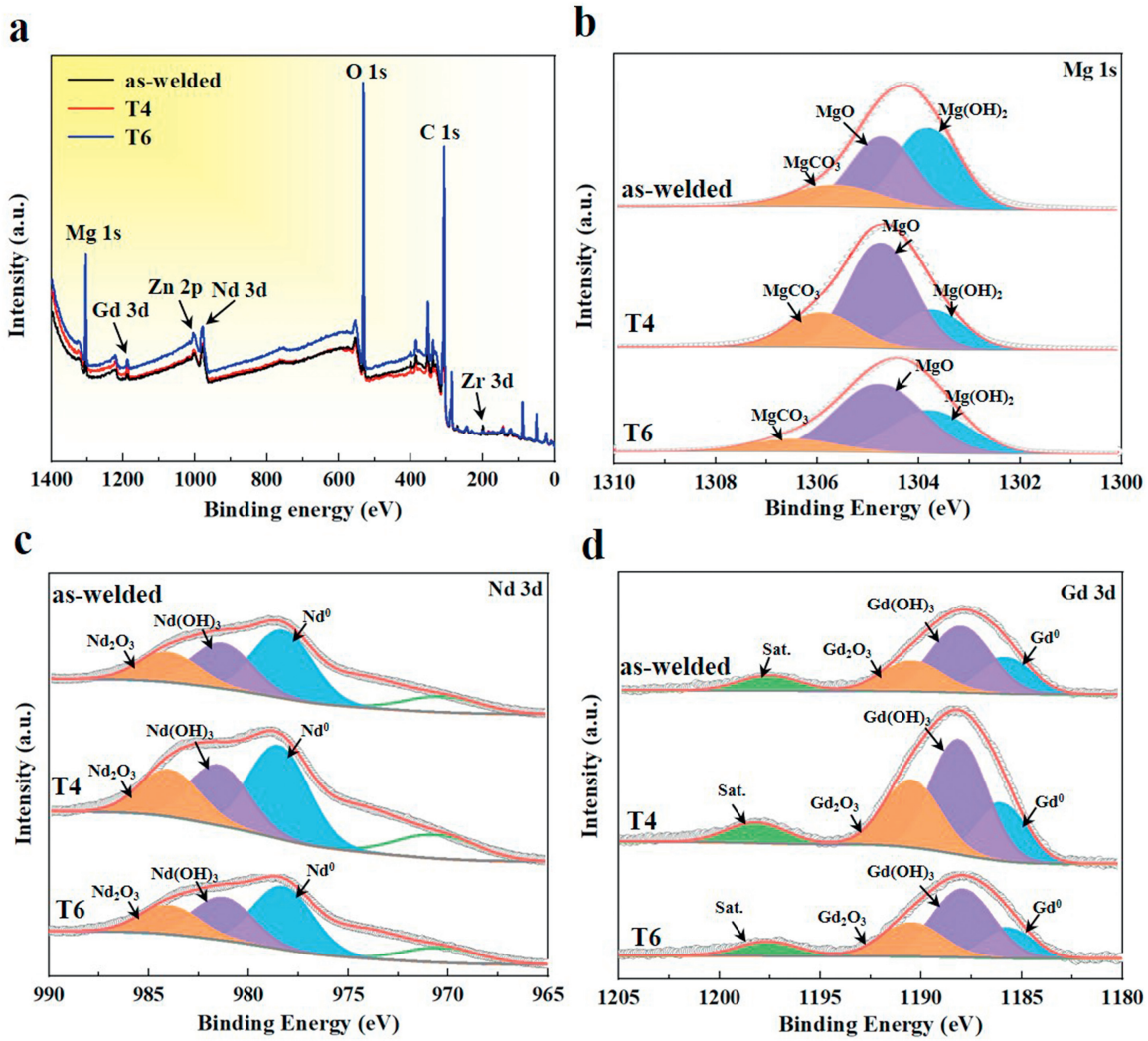

Fig. 15. XPS analysis of corrosion products of FZ in EV33 alloy joints with different heat-treated states: (a) survey scanning spectrum; (b) high-resolution Mg 1s spectrum;(c) high-resolution Nd 3d spectrum; (d) high-resolution Gd 3d spectrum.

T4-treated joint, and 47.4% for the T6-treated joint. That is, a higher proportion of RE atoms are involved in the formation of RE-containing oxides in the T4-treated joint during the immersion test, thus increasing the compactness of the corrosion product layer, as shown in Fig. 11c and d.

3.5. Volta potential difference

SKPFM measurement was carried out to clarify the Volta potential difference (VPD) between the second phase and the α-Mg matrix, as shown in Fig. 16. The result reveals that the potentials of Mg_3(Nd, Gd) eutectic phases, β phase, RE-rich cuboid phases, and Zn–Zr phase are higher than that of the α-Mg matrix. As a result, the α-Mg matrix with lower potential would serve as a micro-anode and be corroded preferentially. In detail, the RE-rich cuboid phases and Mg_3(Nd, Gd) eutectic phases possess an ultra-high average VPD value (∼130 mV), indicating their higher cathode activity than that of β phase (∼30 mV) and Zn–Zr phases (∼70 mV). Therefore, the matrix near the β and Zn–Zr phases could not experience serious galvanic corrosion attack, as shown in Fig. 13. Since the nano-scale precipitates β'' has a similar chemical composition with Mg_3(Nd, Gd) eutectic phases [17,18], it is also electrochemically nobler than the α-Mg matrix.

4. Discussion

4.1. Formation mechanism of corrosion product film

The corrosion product film plays a vital role in the corrosion behavior of EV33 alloy joints, and clarifying its formation mechanism can reveal the film failure mechanisms and provide guidance for surface modification and corrosion control. There exists a significant difference in the composition and morphology of the corrosion product film on the joint surface with different heat-treated states. According to the XRD and XPS analyses, the oxides and hydroxides of Mg and RE are the main components of the corrosion product film. Combined with the microstructure characterization in Fig. 11, it

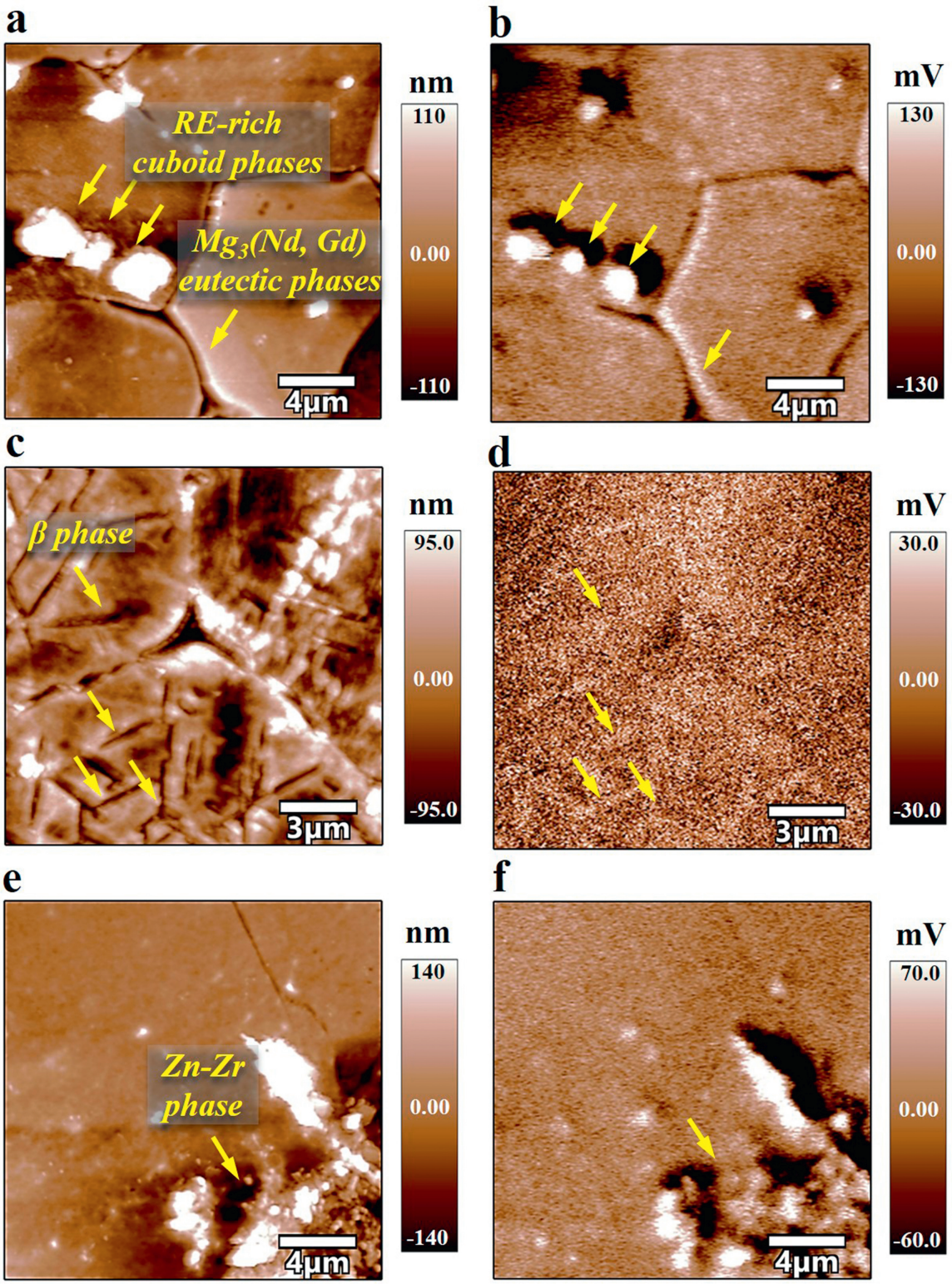

Fig. 16. SKPFM results of the EV33 alloy joints: (a, c, e) Microstructure maps acquired through height sensor; (b, d, f) corresponding surface voltage potential maps.

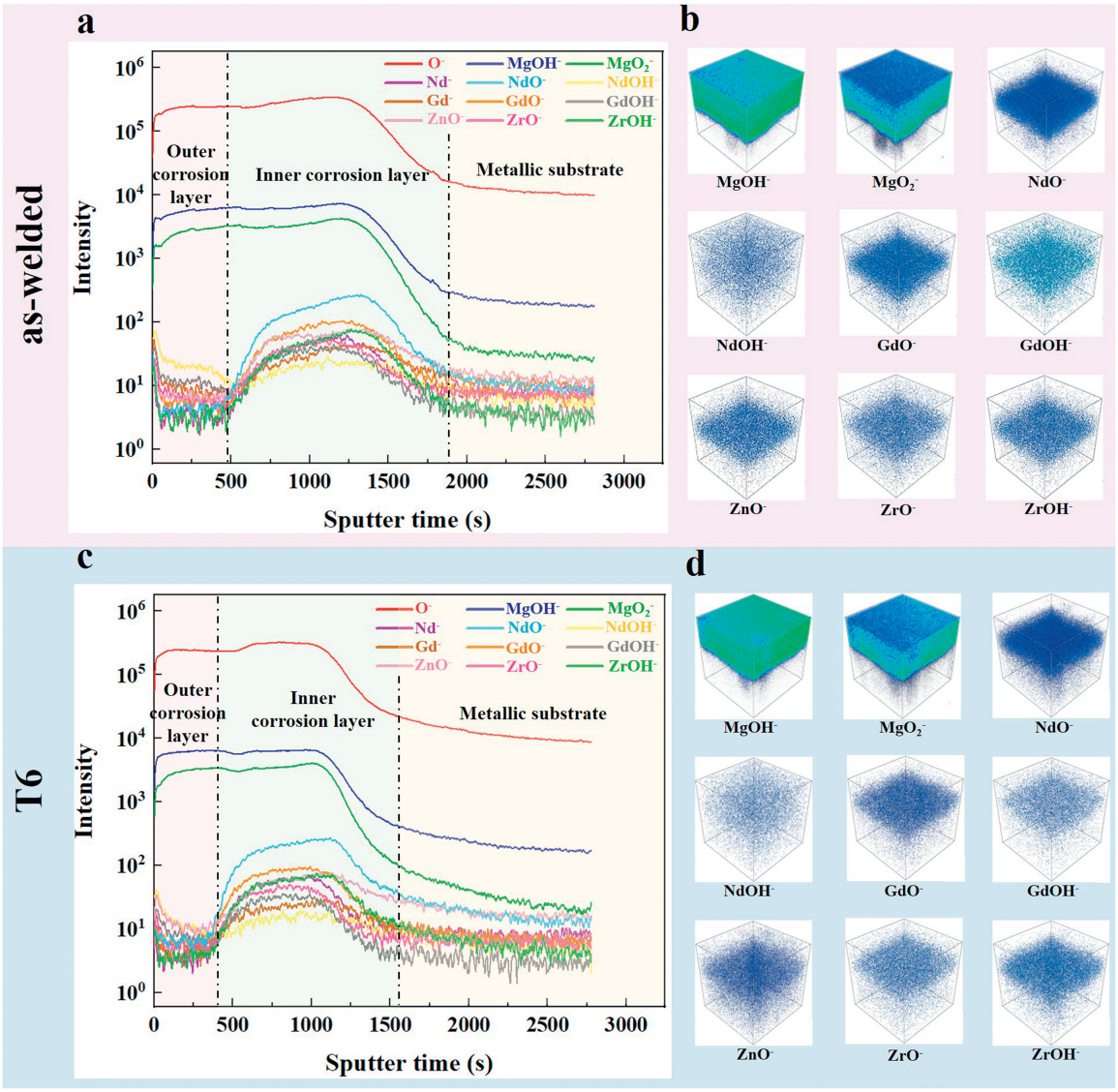

Fig. 17. ToF-SIMS analysis of FZ in the as-welded joint (a and b) and T6-treated joint (c and d): (a, c) ToF-SIMS depth profiles, (b, d) corresponding 3D render of the corrosion product film.

can be found that corrosion products with high RE content are generally in the morphology of dense blade-like flakes, while those with low RE content are characterized with loose globular clusters and some micro-cracks.

To further gain in-depth insight into the structure of the corrosion product film, ToF-SIMS analysis was carried out on the surface of FZ in the as-welded and T6-treated joints, as shown in Fig. 17. Note that the thickness of the corrosion product film is proportional to the ion sputtering time [50,51]. In the direction of thickness, the depth profile of both samples (Fig. 17a and c) predominantly exhibits three regions: the outer corrosion layer, the inner corrosion layer, and the metallic substrate. The outer layer is mainly characterized with intense O^-, MgO_2^-, and $MgOH^-$ signals, which are attributed to the formation of magnesium oxide and hydroxide. The inner layer exhibits a progressively increased intensity of the signals related to ZnO^-, ZrO^-, $ZrOH^-$, Nd-containing ions (Nd^-, NdO^-, and $NdOH^-$), and Gd-containing ions (Gd^-, GdO^-, and $GdOH^-$), revealing an enrichment of oxides and hydroxides of Zn, Zr, and RE. Finally, the O^- signal tends to be stable suggesting that the ion beam has entered the metallic substrate. According to the sputtering time, the corrosion film is markedly thinner on FZ with T6 treatment, suggesting that the substrate erosion of T6-treated FZ is less severe than that of as-welded. In detail, the thickness difference is mainly derived from the inner layer, which indicates that the RE oxides and hydroxides can effectively hinder the corrosion propagation.

The layer composition is better visualized by 3D rendering of corresponding fragment ions (Fig. 17b and d). Results further confirm that magnesium oxide and hydroxide are distributed throughout the corrosion product film, while the oxide and hydroxide of RE, Zn and Zr are mainly located in the inner layer.

It is believed that complex interactions will occur between the corrosive solution and the EV33 alloy joints, which produce significant effects on the composition and structure of the corrosion product film. Therefore, it is of great necessity to discuss the involved interactions. There is a natural oxide film formed on the surface of EV33 alloy joints in the air [52,53], whereas this film is loose and porous thus permitting the access of the Cl^- to the substrate. Then the galvanic corrosion is activated as follows [54,55]:

Cathodic reaction:

$$2H_2O + 2e^- \rightarrow H_2 + 2OH^- \quad (5)$$

Anodic reaction:

$$Mg \rightarrow Mg^{2+} + 2e^- \quad (6)$$

$$RE \rightarrow RE^{3+} + 3e^- \quad (7)$$

Corrosion products:

$$Mg^{2+} + 2OH^- \rightarrow Mg(OH)_2 \quad (8)$$

$$RE^{3+} + 3OH^- \rightarrow RE(OH)_3 \quad (9)$$

Note that the Zn and Zr contents in the current study are extremely low, thus the related reactions could be neglected. Meanwhile, many researchers have confirmed that the adsorbed water molecules on the surface results in the hydroxylation of the natural MgO [26,52,56,57]:

$$MgO + H_2O \rightarrow Mg(OH)_2 \quad (10)$$

According to the Pourbaix diagram [58], Mg and RE oxides are thermodynamically stable in alkaline solutions, which are readily generated by the dehydration of corresponding hydroxides [32,54]:

$$Mg(OH)_2 \rightarrow MgO + H_2O \quad (11)$$

$$2RE(OH)_3 \rightarrow RE_2O_3 + 3H_2O \quad (12)$$

Finally, the reactions between RE elements in the matrix and the already generated $MgO/Mg(OH)_2$ should be considered:

$$2RE + 3MgO \rightarrow 3Mg + RE_2O_3 \quad (13)$$

$$2RE + 3Mg(OH)_2 \rightarrow 3Mg + 2RE(OH)_3 \quad (14)$$

Under the actual experimental temperature of ~25 °C, the Gibbs free energy change (ΔG_T) of reaction (13) can be calculated to be −13.4 kJ/mol and −44.5 kJ/mol for Nd and Gd. In addition, the ΔG_T of reaction (14) is about −243.7 kJ/mol and −230.1 kJ/mol for Nd and Gd, respectively. The negative values of the above-mentioned ΔG_T suggests these reactions are thermodynamically feasible, and Eq. (14) is more favorable than Eq. (13) on account of its lower ΔG_T value.

Based on the discussion above, schematic Fig. 18 is proposed to depict the formation process of the corrosion product film including the following three steps:

(i) As shown in Fig. 18a, the EV33 alloy joint is covered with discontinuous natural oxide film. In 3.5 wt% NaCl solution, the exposed Mg and RE atoms in the substrate are oxidized into Mg^{2+} and RE^{3+} and generate hydroxides. It is noted that a portion of $Mg(OH)_2$ in the outer layer is formed by the hydration of natural MgO. Unfortunately, the generated hydroxides product layer is porous and could not effectively block the penetration of the corrosive solution (Fig. 18b).

(ii) More H_2 bubbles generated at the cathodic sites will escape from the hydroxide layer, resulting in the porosity and cracks within the corrosion film (Fig. 18c). These defects facilitate the penetration of the corrosive solution into the inner substrate. In addition, the hydrolysis reactions produce the oxides stable in alkaline solution (Eqs. (11) and 12) and thus resist pitting breakdown.

(iii) With the inward growth of the corrosion film, more RE oxides and hydroxides can be generated in the inner layer through replacement reaction (Eqs. (13) and 14) on account of the high chemical reactivity of RE elements (Fig. 18d). As reported previously [59,60], there is compressive stress in the oxide film of the RE elements with a Pilling–Bedworth ratio (PBR) between 1 and 2 (1.12 for Nd and 1.29 for Gd), and the film shows a dense structure, resulting in a better oxidation resistance of the base metal. However, the oxide film of Mg element with PBR less than 1 contains tensile stress, lead to the formation of the porous film and a lower oxidation resistance. Therefore, the increased RE_2O_3 in the inner layer can improve the compactness of the corrosion product film and prevent the underlying α-Mg matrix from further corrosion.

4.2. Corrosion behavior of EV33 alloy joints

4.2.1. Different regions in as-welded joint

In terms of the as-welded joint, the corrosion resistance of FZ is higher than that of BM. Combined with the microstructure characterization (Figs. 3 and 4), it can be inferred that the difference in the corrosion performance may be caused by the different distribution of the grain size and second phases.

It is generally believed that grain refinement can lead to a better corrosion resistance of Mg–RE alloys, mainly based on the following reasons [61,62]: (i) finer grains could inhibit pitting initiation by reducing the mismatch stress between α-Mg matrix and the corrosion surface; (ii) More grain boundaries in the grain-refined alloy could act as the barrier to hinder the corrosion propagation. Compared with BM, the grain size of FZ is significantly smaller (~8.2 μm), which results in an enhanced corrosion performance. In addition, the second phase is considered to play a dual role in the corrosion process, which can act as the corrosion barrier or galvanic cathodes accelerating corrosion [48,57,63]. It can be observed from Fig. 12a and b that micro-galvanic corrosion occurs around the eutectics and propagates to the grain interior, suggesting that the eutectics that distributed in the as-welded joint are

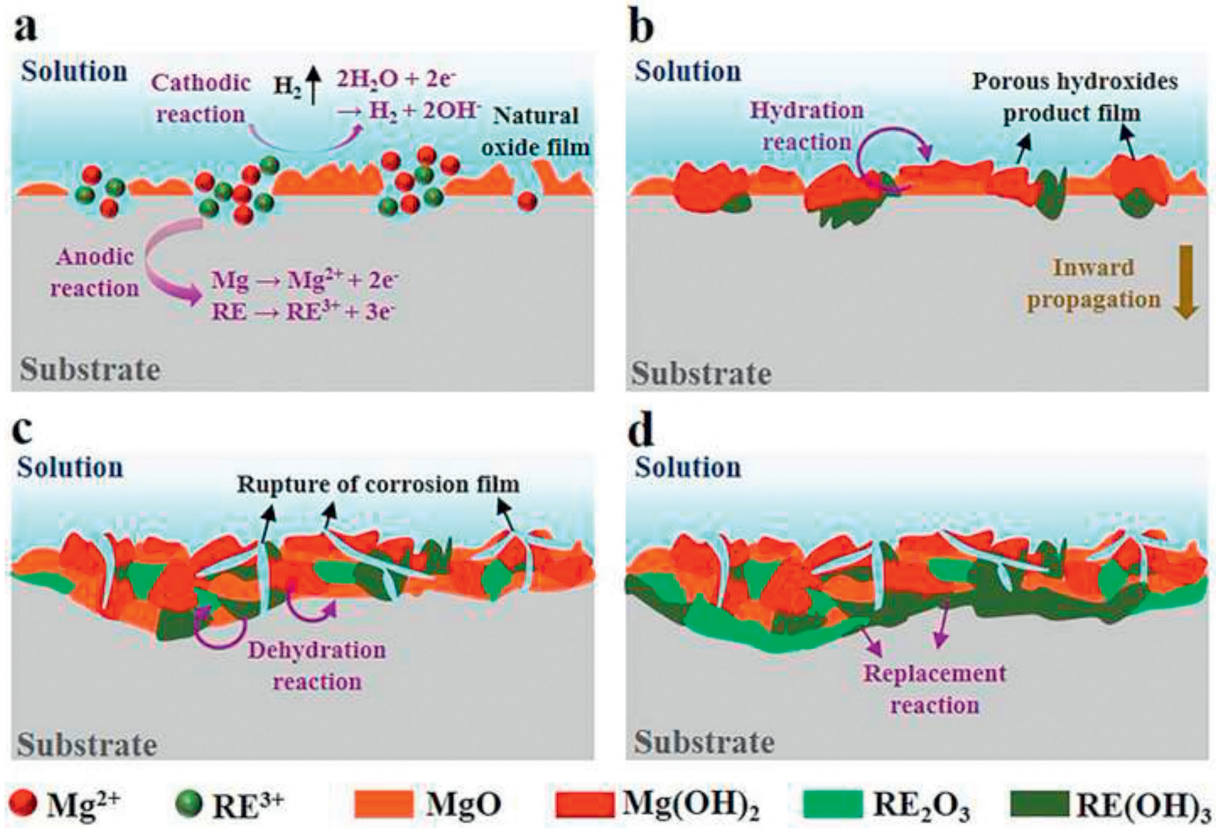

Fig. 18. Schematics of the formation process of the corrosion product film of EV33 alloy joints.

cathodic to the α-Mg matrix and could not effectively impede corrosion progress. It has been reported that the micro-galvanic rate is in proportion to the area ratio of the cathode and anode [64,65], and a larger ratio results in an increased corrosion rate. As shown in Fig. 12b, the eutectics in BM are coarser than those in FZ, which leads to aggravated erosion of the surrounding matrix associated with cracks generated in the corrosion film. Moreover, the uniformly dispersed β phase with a large amount in the grain interior of BM could also form numerous micro-galvanic couples, thus accelerating the galvanic corrosion.

As discussed above, the inferior corrosion performance of BM is attributed to the coarse eutectics and numerous β phase exacerbating galvanic corrosion, as well as the large grain sizes accelerating the corrosion process.

4.2.2. Heat treatment effect

For the as-welded joints, severe micro-galvanic corrosion occurs caused by the Mg_3(Nd, Gd) eutectic phases with relatively large size and high cathode activity (Fig. 13a and b). In addition, the abundant cathodic phases increase the hydrogen evolution rate [57,66], which could induce crack generation within the film and exacerbates localized corrosion. As a result, it is observed that a porous film characterized with loose clusters and deep cracks on the joint surface (Fig. 11a and b), indicating a poor corrosion resistance of the joint in as-welded state.

The dissolution of eutectics and the precipitation of the Zn–Zr phase occurred during T4 treatment, as shown in Fig. 4c and d. Compared with the initial Mg_3(Nd, Gd) eutectics, the Zn–Zr particles in T4 state exhibit smaller sizes and lower Volta potential (~70 mV), resulting in mitigation of the micro-galvanic corrosion (Fig. 13c and d). Although some fine RE-rich sphere/cuboid phases are remained in FZ, their effect on the corrosion performance is minimized because of their small sizes with a low volume fraction [64]. On the other hand, as confirmed by XPS analysis, more RE solute dissolved in the matrix after T4 treatment could be involved in the formation of RE oxides in the corrosive solution. With a high PB ratio and low standard enthalpy [60], RE oxides can greatly improve the compactness and stability of the corrosion product film. As shown in Fig. 11c and d, the relatively uniform film composed of dense blade-like flakes could provide preferable protection against the Cl^-. It is also worth noting that grain growth during T4 treatment is another remarkable factor need to be considered for the corrosion behavior. However, it seems that the negative impact of the grain coarsening on corrosion performance can be offset by the positive effect contributed by the dissolution of cathodic phases and the enhanced protective ability of the corrosion product film, since the lowest corrosion rate is obtained in T4-treated joint.

After T6 treatment, a large quantity of β'' and β' phases are precipitated in the matrix (Fig. 5), which would also act

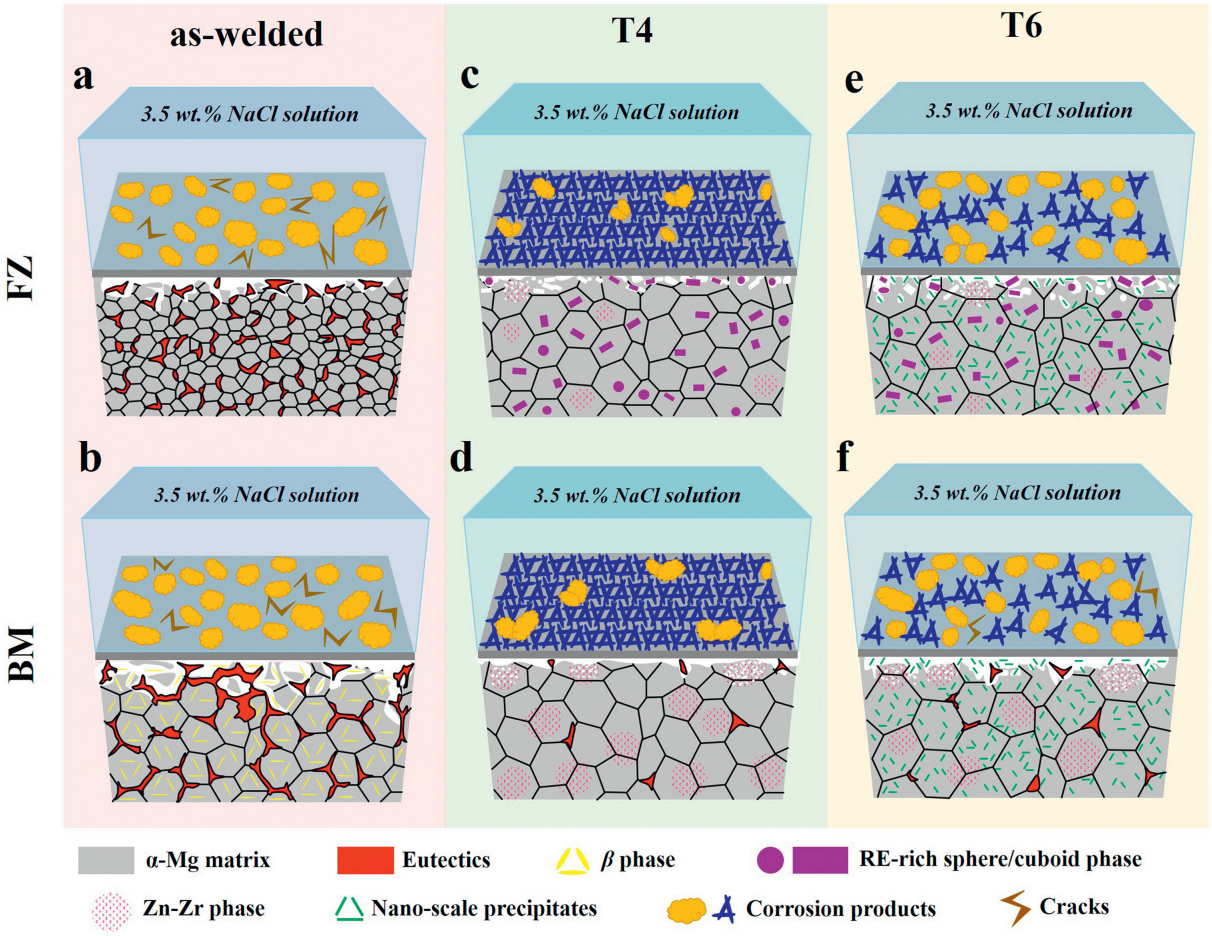

Fig. 19. Schematics of the corrosion behavior of FZ and BM in EV33 alloy joints with different heat-treated states: (a and b) as-welded, (c and d) T4, (e and f) T6.

as micro-cathodes. Note that these precipitates with a diameter of several nanometers cannot provoke severe corrosion damage owing to the extremely small cathode to anode area ratio [64]. However, the reduced RE content in the matrix after aging treatment leads to a lower amount of RE oxides formed in the corrosion products, which is detrimental to the film protection ability (Fig. 11e and f). As a result, the corrosion performance of the T6-treated joint is inferior to that with the T4-treated counterpart. For different regions of the joints after heat treatment, FZ generally exhibits higher corrosion resistance than BM. In addition to the above factors, the Zn–Zr clusters with tens of microns (Fig. 13c–f) as well as a few residual eutectics can also exacerbate the galvanic corrosion of BM.

A schematic is provided in Fig. 19 to better understand the corrosion behavior of EV33 alloy joints with different post-weld heat treatments. The as-welded joint exhibits the highest corrosion rate, on account of the porous corrosion layer and numerous eutectics with high cathodic activity (Fig. 19a and b). In addition, the larger grain sizes, coarser eutectics, and numerous β phase in grain interior make the corrosion resistance of BM inferior to that of FZ. After T4 treatment, the corrosion performance of the joint is significantly improved, owing to the positive effects of the dissolution of cathodic phases and the generation of compact protective film (Fig. 19c and d). The precipitation of nanosized RE-containing phases in T6-treated joint results in a slight increase of micro-galvanic rate and a lower compactness of the protective film (Fig. 19e and f), so a lower corrosion resistance is obtained. The corrosion resistance of BM is slightly inferior to that of FZ in the T4- and T6-treated joints, which is attributed to the large Zn–Zr clusters and residual eutectics in BM.

5. Conclusions

In this work, the effects of different post-weld heat treatments on the microstructure evolution and corrosion behavior of TIG welded EV33 alloys were systematically investigated. The main findings are summarized as follows:

(1) As compared to the FZ in as-welded state, the lower corrosion resistance of cast BM is attributed to its larger grain size and exacerbated galvanic corrosion caused by coarser Mg_3(Nd, Gd) eutectics and numerous β precipitates. In terms of the T4- and T6-treated

joints, the galvanic corrosion resulted from the formed Zn–Zr clusters in BM also leads to a lower corrosion resistance.

(2) The corrosion rate of the EV33 alloy joint in as-welded, T4 and T6 states are 8.43 mm/y, 5.72 mm/y and 7.13 mm/y, respectively. Eutectics with high cathode activity and the porous corrosion film of as-welded joint lead to the highest corrosion rate. The promoted corrosion resistance of T4- and T6-treated joints is derived from the positive effects contributed by the dissolution of eutectics and the formation of a protective layer.

(3) For the as-welded joint, the film is porous with loose globular clusters and micro-cracks, while the layer is compact and uniform with dense blade-like flakes in T4- and T6-treated joints. This is because the content of RE oxides in the corrosion products is greatly increased in T4- and T6-treated joints, which can effectively improve the compactness of the film and hinder the erosion of Cl^-, and a decreased corrosion depth can be obtained.

(4) Different second phases in EV33 alloy joint exhibit distinct Volta potential relative to the α-Mg matrix. The Volta potential of Mg_3(Nd, Gd) and RE-rich cuboid phases is $\sim$130 mV, while that of β and Zn–Zr phases is $\sim$30 mV and $\sim$70 mV respectively. The Zn–Zr phase generated during heat treatment acts as relatively weak micro-cathode, alleviating the micro-galvanic corrosion in comparison with the as-welded joint.

(5) As the major components of the corrosion product film of the EV33 alloy joint, MgO and $Mg(OH)_2$ are distributed throughout the whole layer. However, RE_2O_3 and $RE(OH)_3$ are mainly distributed in the inner layer of the corrosion film, which is generated by the inward propagation of the corrosion and subsequent replacement reactions between RE and $MgO/Mg(OH)_2$.

Data availability

Data will be made available on request.

Declaration of competing interest

The authors declare that they have no known competing financial interests or personal relationships that could have appeared to influence the work reported in this paper.

CRediT authorship contribution statement

Xin Tong: Writing – original draft, Methodology, Data curation, Conceptualization. **Qiman Wang:** Writing – review & editing, Investigation, Data curation. **Guohua Wu:** Supervision, Project administration. **Fangzhou Qi:** Investigation. **Junmin Zhan:** Investigation. **Liang Zhang:** Writing – review & editing, Project administration.

Acknowledgments

This research was supported by the National Natural Science Foundation of China (Nos. U2037601, U2241231, and 51821001).

References

[1] G. Barucca, R. Ferragut, F. Fiori, D. Lussana, P. Mengucci, F. Moia, G. Riontino, Acta Mater. 59 (10) (2011) 4151–4158.
[2] X. Tong, G. Wu, M. Sun, Q. Wang, L. Zhang, W. Liu, J. Mater. Sci. Technol. 173 (20) (2024) 202–217.
[3] G. Wu, X. Tong, C. Wang, R. Jiang, W. Ding, J. Magn. Alloys 11 (10) (2023) 3463–3483.
[4] J. Zhang, S. Liu, R. Wu, L. Hou, M. Zhang, J. Magn. Alloys 6 (3) (2018) 277–291.
[5] J. Liu, B. Yin, F. Song, B. Liu, B. Peng, P. Wen, Y. Tian, Y. Zheng, X. Ma, C. Wang, J. Magn. Alloys 12 (3) (2024) 940–953.
[6] G.S. Pereira, O.M. Prada Ramirez, P.R.T. Avila, J.A. Avila, H.C. Pinto, M.H. Miyazaki, H.G. de Melo, W.W. Bose Filho, Corros. Sci. 206 (2022) 110527.
[7] J. Zhang, S. Han, Y. Sun, X. Chen, P. Chen, Z. Li, G. Huang, F. Pan, Mater. Sci. Eng.: A 880 (2023) 145329.
[8] K. Luo, L. Zhang, G. Wu, W. Liu, W. Ding, J. Magn. Alloys 7 (2) (2019) 345–354.
[9] X. Tong, G. Wu, M.A. Easton, M. Sun, Q. Wang, L. Zhang, Addit. Manuf. 67 (2023) 103487.
[10] Q. Wang, G. Wu, X. Tong, Mater. Lett. 326 (2022) 132922.
[11] S.Y. Jian, C.Y. Yang, J.K. Chang, Appl. Surf. Sci. 510 (2020) 145385.
[12] D. Zhang, D. Qiu, S. Zhu, M. Dargusch, D. StJohn, M. Easton, Scr. Mater. 183 (2020) 12–16.
[13] F. Qi, X. Zhang, G. Wu, W. Liu, X. He, W. Ding, Mater. Sci. Eng.: A 813 (2021) 141172.
[14] Q. Wang, X. Tong, G. Wu, J. Zhan, F. Qi, L. Zhang, W. Liu, Mater. Sci. Eng.: A 869 (2023) 144816.
[15] H. Xie, G. Wu, L. Zhang, X. Tong, R. Jiang, W. Liu, J. Magn. Alloys (2023), doi:10.1016/j.jma.2023.01.014.
[16] H. Xie, G. Wu, X. Tong, R. Jiang, L. Zhang, W. Liu, Z. Li, Mater. Charact. 194 (2022) 112442.
[17] H. Xie, G. Wu, X. Zhang, W. Liu, W. Ding, Mater. Charact. 175 (2021) 111076.
[18] F. Qi, X. Zhang, G. Wu, W. Liu, L. Wen, H. Xie, S. Xu, X. Tong, Mater. Charact. 183 (2022) 111630.
[19] J. Huang, W. Pan, J. Chen, Y. Shao, M. Yang, Y. Zhang, J. Manuf. Process. 36 (2018) 405–416.
[20] D.H. Meng, B. Zhou, D. Wu, Y.Q. Ma, R.S. Chen, P.J. Li, Int. J. Metalcast. 13 (2) (2018) 345–353.
[21] X. Tong, G. Wu, L. Zhang, Y. Wang, W. Liu, W. Ding, J. Magn. Alloys 10 (1) (2022) 180–194.
[22] Y. Ma, G. Chen, Q. Yin, G. Zhang, B. Zhang, X. Leng, Mater. Sci. Eng.: A 853 (2022) 143608.
[23] G. Zhang, X. Tong, G. Wu, L. Zhang, H. Sui, X. Zhang, Mater. Sci. Eng.: A 821 (2021) 141577.
[24] C. Meng, J. Yang, Z. Zhang, Z. Song, L. Zhang, Y. Jiang, Mater. Charact. 203 (2023) 113088.
[25] S. Chai, Q. Dai, S. Zhong, Q. Yang, L. Yin, D. Zhang, J. Feng, Q. Li, J. Mater. Sci. Technol. 182 (2024) 176–186.
[26] P.W. Chu, E.A. Marquis, Corros. Sci. 101 (2015) 94–104.
[27] V. Kodetová, B. Smola, I. Stulíková, H. Kudrnová, M. Vlach, V. Neubert, J. Therm. Anal. Calorim. 138 (3) (2019) 2167–2174.
[28] S. Liang, D. Guan, X. Tan, Mater. Des. 32 (3) (2011) 1194–1199.
[29] P. Maier, N. Lauth, C.L. Mendis, M. Bechly, N. Hort, Jom 71 (4) (2019) 1426–1435.
[30] L.l. Shi, Y. Huang, L. Yang, F. Feyerabend, C. Mendis, R. Willumeit, K.U. Kainer, N. Hort, J. Mech. Behav. Biomed. Mater. 47 (2015) 38–48.
[31] H. Xu, X. Deng, X. Zhang, K. Zhang, Y. Liu, S. Li, J. Wuhan Univ. Technol.-Mater. Sci. Ed. 30 (4) (2015) 796–803.

[32] K. Ma, J. Wang, W. Zheng, Y. Peng, C. Dai, Y. Pan, Y. Wang, D. Wang, J. Wang, Y. Ma, Corros. Sci. 208 (2022) 110689.
[33] Z. Shi, M. Liu, A. Atrens, Corros. Sci. 52 (2) (2010) 579–588.
[34] W.Z. Wang, D. Wu, R.S. Chen, Y. Qi, H.Q. Ye, Z.Q. Yang, J. Alloys Compd. 832 (2020) 155016.
[35] J.-F. Nie, Metallur. Mater. Trans. A 43 (11) (2012) 3891–3939.
[36] J. Li, E.-T. Han, Biochem. Biophys. Res. Commun. 426 (1) (2012) 1–6.
[37] D. Wang, P. Fu, L. Peng, Y. Wang, W. Ding, Mater. Charact. 153 (2019) 157–168.
[38] J. Li, Q. Jiang, H. Sun, Y. Li, Corros. Sci. 111 (2016) 288–301.
[39] W. Ci, X. Chen, Y. Sun, X. Dai, G. Zhu, D. Zhao, F. Pan, J. Mater. Sci. Technol. 158 (2023) 31–42.
[40] D. Song, A. Ma, J. Jiang, P. Lin, D. Yang, J. Fan, Corros. Sci. 52 (2) (2010) 481–490.
[41] C. Dai, J. Wang, Y. Pan, K. Ma, Y. Peng, Y. Wang, D. Wang, C. Ran, J. Wang, Y. Ma, Corros. Sci. 220 (2023) 111227.
[42] K. Zhang, C. Wang, S. Liu, K. Guan, M.X. Li, L.Y. Zhang, H.Y. Wang, Corros. Sci. 220 (2023) 111254.
[43] K. Zhang, C. Wang, D.-W. Wang, M.X. Li, Y.L. Ma, Z.M. Hua, L.Y. Zhang, J. Li, H.Y. Wang, Corros. Sci. 213 (2023) 110971.
[44] S. Yin, W. Duan, W. Liu, L. Wu, J. Yu, Z. Zhao, M. Liu, P. Wang, J. Cui, Z. Zhang, Corros. Sci. 166 (2020) 108419.
[45] X. Liu, J. Xue, S. Liu, Mater. Des. 160 (2018) 138–146.
[46] T. Zhang, G. Meng, Y. Shao, Z. Cui, F. Wang, Corros. Sci. 53 (9) (2011) 2934–2942.
[47] Z. Zhang, G. Wu, A. Atrens, W. Ding, J. Magn. Alloys 8 (1) (2020) 301–317.
[48] J. Chang, X. Guo, S. He, P. Fu, L. Peng, W. Ding, Corros. Sci. 50 (1) (2008) 166–177.
[49] H. Zhang, Y. Zhao, J. Liu, J. Xu, D. Guo, C. Li, X. Zhou, P. Yang, S. Zhang, Int. J. Electrochem. Sci. 18 (6) (2023) 100160.
[50] H. Ardelean, A. Seyeux, S. Zanna, F. Prima, I. Frateur, P. Marcus, Corros. Sci. 73 (2013) 196–207.
[51] A.I. Ikeuba, Appl. Surf. Sci. Adv. 15 (2023) 100410.
[52] M. Esmaily, J.E. Svensson, S. Fajardo, N. Birbilis, G.S. Frankel, S. Virtanen, R. Arrabal, S. Thomas, L.G. Johansson, Prog. Mater. Sci. 89 (2017) 92–193.
[53] Y. Song, E.H. Han, K. Dong, D. Shan, C.D. Yim, B.S. You, Corros. Sci. 88 (2014) 215–225.
[54] C. Dai, J. Wang, Y. Pan, K. Ma, Y. Peng, J. Ren, Y. Wang, D. Wang, J. Wang, Y. Ma, Corros. Sci. 210 (2023) 110806.
[55] J. Zhang, B. Jiang, Q. Yang, D. Huang, A. Tang, F. Pan, Q. Han, J. Alloys Compd. 849 (2020) 156619.
[56] L.G. Bland, K. Gusieva, J.R. Scully, Electrochim. Acta 227 (2017) 136–151.
[57] S. Yin, W. Duan, W. Liu, L. Wu, J. Bao, J. Yu, L. Li, Z. Zhao, J. Cui, Z. Zhang, Corros. Sci. 177 (2020) 108962.
[58] M. Pourbaix, J. Electroanal. Chem. 13 (4) (1967) 471.
[59] M. Ciumag, M. Gibilaro, L. Massot, R. Laucournet, P. Chamelot, J. Fluor. Chem. 184 (2016) 1–7.
[60] Y.M. Kim, C.D. Yim, H.S. Kim, B.S. You, Scr. Mater. 65 (11) (2011) 958–961.
[61] M. Mohammadi Zerankeshi, R. Alizadeh, E. Gerashi, M. Asadollahi, T.G. Langdon, J. Magn. Alloys 10 (7) (2022) 1737–1785.
[62] J. Xie, J. Zhang, Z. You, S. Liu, K. Guan, R. Wu, J. Wang, J. Feng, J. Magn. Alloys 9 (1) (2021) 41–56.
[63] G.L. Song, 1 - Corrosion behavior and prevention strategies for magnesium (Mg) alloys, in: G.-L. Song (Ed.), Corrosion Prevention of Magnesium Alloys, Woodhead Publishing2013, pp. 3–37.
[64] J.X. Chen, M. Gao, L.L. Tan, K. Yang, Rare Metals. 38 (6) (2019) 532–542.
[65] R. Zeng, K.U. Kainer, C. Blawert, W. Dietzel, J. Alloys Compd. 509 (13) (2011) 4462–4469.
[66] Y.J. Li, M.X. Li, Z.M. Hua, B.Y. Wang, Y. Gao, H.Y. Wang, Corros. Sci. 211 (2023) 110861.